

The Star Formation History of NGC 6822

Ted K. Wyder

California Institute of Technology, Mail Code 405-47, 1200 E California Blvd, Pasadena, CA 91125

wyder@srl.caltech.edu

ABSTRACT

Images of five fields in the Local Group dwarf irregular galaxy NGC 6822 obtained with the *Hubble Space Telescope* in the F555W and F814W filters are presented. Three of the fields lie mostly within the central bar of NGC 6822 where most of the sites of current star formation are concentrated while two other fields sample more of the outer regions of the galaxy. Photometry for the stars in these images was extracted using the Point-Spread-Function fitting program HSTPHOT/MULTIPHOT. The resulting color-magnitude diagrams reach down to $V \approx 26$, a level well below the red clump, and were used to solve quantitatively for the star formation history of NGC 6822. Assuming that stars began forming in this galaxy from low-metallicity gas and that there is little variation in the metallicity at each age, the distribution of stars along the red giant branch is best fit with star formation beginning in NGC 6822 12-15 Gyr ago. The best-fitting star formation histories for the old and intermediate age stars are similar among the five fields and show a constant or somewhat increasing star formation rate from 15 Gyr ago to the present except for a possible dip in the star formation rate from 3 to 5 Gyr ago. The main differences among the five fields are in the higher overall star formation rate per area in the bar fields as well as in the ratio of the recent star formation rate to the average past rate. These variations in the recent star formation rate imply that stars formed within the past 0.6 Gyr are not spatially very well mixed throughout the galaxy. The star formation histories in conjunction with a galaxy evolution code are used to infer the evolution of the integrated absolute magnitude of NGC 6822 as a function of look-back time and redshift. The results indicate that galaxies with star formation histories similar to that determined for NGC 6822 would have an absolute magnitude of $M_B = -15.7$ at a redshift $z = 0.6$, well below the detection limit of the current redshift surveys, and therefore are most likely not contributing to the evolving galaxy population detected in deep redshift surveys.

Subject headings: galaxies: individual (NGC 6822), galaxies: evolution, galaxies: irregular, galaxies: stellar content, galaxies: Local Group

1. Introduction

The dwarf galaxies of the Local Group provide excellent laboratories with which to study galaxy evolution. Dwarf galaxies are in general useful in studying stellar populations and galaxy evolution in the absence of the complicating effects of density waves common in giant disk galaxies. Dwarf galaxies have been found at a variety of distances from giant galaxies, allowing us to investigate the importance of environment in their evolution. Their low metallicities allow us to study how galaxies form stars under conditions similar to that at high redshift in larger galaxies. The proximity of Local Group galaxies means that we can study them in greater detail than for any other galaxies. For recent comprehensive reviews of the properties of Local Group galaxies, see Hodge et al. (1989), Mateo (1998), and van den Bergh (2000), among others.

Detailed studies of nearby dwarf galaxies are also relevant to understanding the nature of the faint blue galaxies detected in deep imaging and redshift surveys (Ellis 1997). The redshift surveys described by Lilly et al. (1995) and Ellis et al. (1996) show that the faint blue galaxies lie at redshifts of $0.2 < z < 1.0$, have strong [OII] emission indicative of active star formation, and contribute to a steepening of the faint end slope of the luminosity function. One model that has been proposed to explain these observations is that the evolving population in these surveys is comprised of dwarf galaxies that form all of their stars in a single burst of star formation lasting $\sim 10^7$ years at a redshift of $z \sim 1$ (Babul & Rees 1992; Babul & Ferguson 1996). While none of the star formation histories (SFHs) of Local Group dwarf galaxies yet observed fit exactly this scenario, it may be possible that some of the Local Group dwarfs may be the low redshift counterparts to the evolving population detected in the redshift surveys. By determining the SFHs of as many nearby galaxies as possible and comparing them with the properties of distant galaxies, we should be able to come to a better understanding of the nature of the faint blue galaxies and their low redshift counterparts.

With a few exceptions, the dwarf galaxies of the Local Group can be classified into early type dwarf ellipticals and dwarf spheroidals and late type dwarf irregulars. The dwarf ellipticals and dwarf spheroidals are gas poor, have no current star formation and tend to be concentrated close to M31 and the Milky Way while the dwarf irregulars are gas rich, are currently forming stars and have a more uniform distribution throughout the Local Group (Mateo 1998; van den Bergh 2000). Mateo (1998) presented a summary of observations of a number of Local Group galaxies which illustrated the variety of SFHs observed. While none of the dwarf galaxies share the exact same SFH, there are a few trends that have emerged. While it had once been assumed that all dwarf spheroidals contained exclusively old populations, it has become clear that there are many dwarf spheroidals, such as Carina (Smecker-Hane et al. 1994), that have undergone multiple star formation episodes resulting in a dominant population of intermediate age stars. On the other hand, there is increasing evidence that many dwarf irregular galaxies, such as NGC 6822 (Gallart et al. 1996a) and IC 1613 (Cole et al. 1999), contain significant intermediate age and old stellar populations. The only dwarf irregular known to be composed of almost entirely young (< 1 Gyr old) stars is Leo A (Tolstoy et al. 1998) while Draco and Ursa Minor are the only dwarf spheroidals

known which contain only very old stars (Grillmair et al. 1998; Mighell & Burke 1999). Despite the substantial progress made in understanding the evolution of dwarf galaxies, the nature of the relationship between dwarf spheroidal and dwarf irregular galaxies remains unknown.

NGC 6822 in particular is a Local Group dwarf irregular galaxy that has been the subject of numerous observational studies at a variety of wavelengths. In his historic paper, Hubble (1925) presented his discovery of Cepheids in this galaxy which made NGC 6822 the first object recognized as a truly extragalactic object well outside the Milky Way. Since then, the distance to NGC 6822 has become fairly well established in that it has been measured both using the Cepheid period-luminosity relation and the tip of the red giant branch. McAlary et al. (1983) obtained a distance modulus of $(m - M)_0 = 23.47 \pm 0.11$ based upon their *H*-band photometry of nine Cepheids in NGC 6822. Using *BVRI* photometry to recalibrate the Cepheid light curves originally measured by Kayser (1967) and assuming a distance modulus to the LMC of 18.5, Gallart et al. (1996a) derived a distance modulus of 23.49 ± 0.08 (500 kpc), the value that I have adopted in the analysis presented in this paper. These Cepheid distances are consistent with the tip of the red giant branch distance moduli of 23.46 and 23.40 obtained by Lee et al. (1993) and Gallart et al. (1996a), respectively.

Since it lies at a rather low Galactic latitude of $b = 18.4^\circ$, the foreground reddening toward NGC 6822 is significant and has a value of $E(B - V) = 0.24$ (Schlegel et al. 1998). The optical structure of NGC 6822 consists of a bar oriented roughly north-south containing most of the sites of current star formation while the outer regions surrounding the bar contain a population of fainter, redder and most likely somewhat older stars (Hodge 1977; Hodge et al. 1991). Studies of OB stars in NGC 6822 indicate that the reddening increases from the foreground value in the outer regions to values of $E(B - V) = 0.45$ in the vicinity of the bar (Massey et al. 1995). There are numerous H II regions concentrated in the bar which have been studied most recently by Hodge et al. (1988, 1989) and Collier et al. (1995). Spectra of some of the H II regions in NGC 6822 indicate oxygen abundances substantially less than solar (Peimbert & Spinrad 1970; Smith 1975; Lequeux et al. 1979; Pagel et al. 1980; Skillman et al. 1989b). In particular, Skillman et al. (1989b) derived an oxygen abundance of $O/H = (1.6 \pm 0.4) \times 10^{-4}$ which corresponds to an overall metallicity of 20% solar or a fraction by mass of metals of $Z = 0.004$. This places NGC 6822 near the average metallicity-luminosity relationship for dwarf galaxies (Skillman et al. 1989a). NGC 6822 contains a large reservoir of H I gas that extends over a region much larger than the optical diameter of $D_{25} = 15.5'$ (Davies 1972; Roberts 1972; Gottesman & Weliachew 1977; de Blok & Walter 2000). Using their best-fitting inclination of $69^\circ \pm 3$, Gottesman & Weliachew (1977) derived a total mass for NGC 6822 from their H I rotation curve of $1.4 \times 10^9 M_\odot$ within a radius of $18'$, or 2.6 kpc. The far infra-red emission in NGC 6822 as detected by the IRAS satellite has been analyzed by Gallagher et al. (1991) and Israel et al. (1996). Despite its low metallicity, CO emission associated with molecular clouds in NGC 6822 has been detected (Wilson 1992a, 1994; Israel 1997).

Beginning with Kayser (1967), there have been numerous studies of the stellar content of NGC 6822. Armandroff & Massey (1985) discovered 12 Wolf-Rayet stars in NGC 6822 while Hoessel & Anderson (1986) and Wilson (1992b) have determined the blue star luminosity function. The OB

associations in this galaxy have been cataloged and studied by Hodge (1977) and Wilson (1992b). Many carbon stars were discovered by Cook et al. (1986) in two fields at either end of the bar, providing the first evidence for a significant intermediate-age population in NGC 6822. One of the star clusters in NGC 6822, Hubble VII, is likely similar in age and metallicity to the Milky Way globular clusters while the clusters Hubble VI and Hubble VIII are probably similar to the “populous clusters” observed in the Magellanic Clouds (Cohen & Blakeslee 1998; Wyder et al. 2000; Chandar et al. 2000). In addition there are numerous smaller open clusters cataloged by Hodge (1977).

Recently, there have been two attempts to quantify the SFH of NGC 6822 based upon color-magnitude diagrams (CMDs) derived from ground-based data. Using BV photometry of two fields in the vicinity of the bar reaching down to $V \simeq 23.5$, Marconi et al. (1995) derived information about the recent (< 1 Gyr) SFH by comparing the observed CMD with synthetic diagrams. They found evidence for a more continuous star formation rate (SFR) in one of the fields while the other is better fit with a SFH containing two star formation episodes each lasting a few hundred Myr. Gallart et al. (1996a,b,c) investigated the SFH using VI CMDs reaching down to $I \simeq 22$ that covered an $11.2' \times 10.4'$ area centered on the bar. By comparing the observed CMDs with model diagrams, Gallart et al. (1996a) found that NGC 6822 most likely began forming stars 12-15 Gyr ago from low metallicity gas. The observed CMDs could also be consistent with star formation beginning only 6-9 Gyr ago if prompt metal enrichment occurred in the galaxy. Over the past few Gyrs, a SFR that is constant or declining fits the observations. For the most recent SFH, Gallart et al. (1996b) found evidence for an enhancement in the field SFR in the last 100-200 Myr with the enhancement being greater in the center of the bar than in the outer regions and greater still at the ends of the bar. Hodge (1980) also found evidence for an enhancement in the cluster formation rate 75-100 Myr ago using cluster ages determined by the magnitude of the brightest star in each cluster.

The main goal of this paper is the analysis of the stellar populations and star formation history of NGC 6822 based mainly upon five *Hubble Space Telescope (HST)* pointings within the galaxy. The higher resolution *HST* data of the fields presented here is essential in coming to a better understanding of the evolutionary history of this galaxy and are a natural compliment to the previous more spatially complete but shallower ground-based data. With this new data, the variation in the star formation history with position in NGC 6822 can be investigated as well as the age of the oldest stars. Knowledge of the star formation history of NGC 6822 is an essential step in comparing the evolutionary history of NGC 6822 with other nearby dwarf galaxies as well as understanding the nature of the evolving population of galaxies detected in deep redshift surveys. This paper is organized as follows. §2 describes the data and photometry of the five fields. In §3, I describe the methods used to extract information about the star formation history of each field while the results of these analyses are presented in §4. The main conclusions of this paper are summarized in §5.

2. Observations and Photometry

2.1. Observations

The observations presented here consist of images of five fields in NGC 6822 taken with the WFPC2 aboard *HST*. The locations of these fields in NGC 6822 are shown in Figure 1. In four of the fields, the PC chip is centered on one of the clusters H IV, H VI, H VII or H VIII originally identified by Hubble (1925) while the fifth field is centered on the open cluster C25 from the list in Hodge (1977). All five fields were imaged through the F555W and F814W filters which are similar to the standard *V* and *I* filters, respectively. Two exposures per field in each filter were obtained to assist in removal of cosmic rays. I obtained the images from the Space Telescope Science Institute after the data were processed by the standard WFPC2 calibration pipeline described in detail in Holtzman et al. (1995a). The Hubble cluster fields are a part of *HST* program 6813 proposed by Paul Hodge (PI), Mario Mateo and Toby Smith while the C25 observations are a part of *HST* program 8314 proposed by Paul Hodge (PI), Eugene Magnier, Andrew Dolphin and Rupali Chandar. A summary of the observations is shown in Table 1. The analysis of the clusters appearing in the PC images has already been presented in Wyder et al. (2000).

2.2. HSTPHOT/MULTIPHOT photometry

To obtain photometry for the stars in these images, I relied on a new PSF-fitting photometry package, HSTPHOT (Dolphin 2000b), kindly provided to me by the author. HSTPHOT is similar in many respects to other PSF-fitting stellar photometry programs such as DAOPHOT/ALLSTAR (Stetson 1994) and DoPhot (Schecter et al. 1993). HSTPHOT is designed specifically for use with *HST* WFPC2 data and relies on a library of Tiny Tim PSFs for the PSF-fitting. The PSFs are sampled on a 200×200 pixel grid on each chip to account for spatial variations in the stellar shapes. The main innovations of this software are that it subsamples the PSF on a 5×5 grid within each PC pixel and on a 10×10 grid within each WF pixel and accounts for the subpixel variation in the quantum efficiency. (See Dolphin 2000b for a detailed description of HSTPHOT). An earlier version of this software was used by Hodge et al. (1999) and Dolphin (2000a) to analyze WFPC2 observations of the Local Group dwarf galaxy WLM (DDO 221).

Before performing the photometry, I averaged together the two individual exposures per cluster taken in each filter using a routine included in the HSTPHOT package, *crclean*. Cosmic rays are rejected in this program using an algorithm nearly identical to that implemented in the IRAF task *crrej*. Before performing the photometry, the data quality files that accompany the data were used to replace the value in bad pixels with -100 DN so that they will not be considered when extracting the photometry.

The HSTPHOT package includes the program MULTIPHOT which actually performs the PSF-fitting. MULTIPHOT differs from other photometry programs in that it solves for the center

and magnitudes for each star in all of the input images in all filters simultaneously. I have used MULTIPHOT to analyze the field stars in all five fields. MULTIPHOT modifies the PSF for each image to account for any focus variations that may cause the real PSF to deviate from the Tiny Tim model.

The cosmic-ray cleaned images output by *cclean* in each filter were input into MULTIPHOT. Stars were identified using a minimum signal-to-noise threshold of 3. In calculating a magnitude for each star in each filter, MULTIPHOT corrects for the effects of the geometric distortion on the photometry as well as the 34th row error. The counts were also corrected for the charge-transfer-efficiency (CTE) effect using the results presented in Dolphin (2000c). This CTE correction used here is similar to that determined by Whitmore et al. (1999).

Aperture corrections were determined automatically by MULTIPHOT by measuring aperture magnitudes within a radius of $0.5''$ for several of the brightest stars on each chip from an image in which all of the other stars have been subtracted. Then a mean aperture correction for each chip and filter was determined by averaging the differences between the PSF-fit and aperture magnitudes. The standard deviations of the aperture minus the PSF-fit magnitudes in all of the fields are in the range of 0.02 – 0.05 magnitudes. I conservatively adopt this as the likely uncertainty in the aperture corrections and it probably represents the dominant source of error in the overall photometry zeropoint.

The instrumental F555W and F814W aperture-corrected magnitudes were then calibrated and transformed to standard V and I using the transformations presented in Dolphin (2000b). The color terms in that paper are those originally determined by Holtzman et al. (1995b) while the zeropoints have been redetermined via comparison of WFPC2 exposures of the globular clusters ω Cen and NGC 2419 with ground-based $UBVRI$ data. The V and I zeropoints assumed here differ from the commonly used Holtzman et al. (1995b) zeropoints by -0.009 and 0.012 magnitudes in V and I , respectively, where the differences are in the sense of Holtzman et al. (1995b) minus Dolphin (2000b). The new calibration also incorporates new determinations of the gain for each chip which result in zeropoint differences of -0.044 , 0.007 , -0.007 and -0.006 mag relative to the Holtzman et al. (1995b) results for the PC, WF2, WF3 and WF4, respectively.

MULTIPHOT calculates two parameters for each star, χ and *sharp*, which are very similar to parameters output by DAOPHOT and can be used to eliminate poorly fit stars as well as non-stellar objects. χ is a measure of the overall goodness of the PSF fit while *sharp* indicates whether the object may be a hot pixel or a background galaxy. An object that is completely flat would have a *sharp* value of -1 while an object sharper than the PSF would have a positive value. In less crowded fields, well fit stars should have $\chi < 2.5$ (Dolphin 2000b). For the very crowded fields analyzed here, I have adopted a somewhat larger χ limit to insure that the photometry is as complete as possible. Any biases introduced by the adopted χ cut should be accounted for by the artificial stars tests described below. Only stars with $\chi < 6$ and $-0.5 < \text{sharp} < 0.5$ in both filters were retained for the final photometry list. These same limits were used for all five fields. The resulting V, I

color-magnitude diagrams for all stars detected in the WF chips in each field are plotted in Figure 2. There are a total of 34,285, 47,872, 45,312, 32,303 and 27,823 stars detected in the three WF chips in the H IV, H VI, H VII, H VIII and C25 fields, respectively. In each of the panels of Figure 2, the data are plotted as individual points in those parts of the diagrams where the density of points is low. However, in those areas of each CMD where the density of stars is greater than 20 decimag^{-2} , the data are plotted as contours. All of the CMDs throughout the remainder of this paper are plotted in the same manner.

2.3. Artificial Star Tests

The analysis of the CMDs described in the remaining sections requires a quantitative assessment of the observational effects on the observed CMD. This has been done using the results of a series of artificial star tests performed on each of the five fields with routines within the MULTIPHOT program. The artificial stars were given random magnitudes and colors in the range $20 < V < 29$ and $-0.5 < V - I < 3.5$ for the four Hubble cluster fields while the artificial stars in the C25 field were chosen to have magnitudes in the range $18 < V < 28$ due to the shorter exposure time. In each field the total number of stars added ranged between 9×10^5 and 1.1×10^6 stars per field. Positions for the stars were chosen to mimic the distribution of light in each image. The artificial stars were then convolved with the appropriate PSF for its chip, filter and position and the appropriate amount of noise added. Then the artificial stars were detected and measured using the same algorithms as for the observed data. Since the artificial stars follow the model PSF exactly (with the addition of random Poisson noise), it is important to note that these completeness tests only simulate the uncertainties associated with the crowding, Poisson noise and sky determination and would not be able to account for any uncertainties due to any possible mismatch between the model and observed PSF.

An input artificial star was classified as recovered if it was recovered in both V and I with $\chi < 6$ and $-0.5 < \text{sharp} < 0.5$ in both images. The results of the artificial star tests for each field are shown in Figure 3. Each panel of this figure shows the fraction of artificial stars recovered as a function of the input V magnitude. The completeness results are plotted separately for three $V - I$ bins. In each field, the completeness for the red stars is greater than in the blue. At the bright end, the completeness is about 95% in all fields. For fainter magnitudes, the completeness falls off more quickly with increasing magnitude for the more crowded fields H VI and H VII than in the H IV and H VIII pointings despite the nearly identical exposure times in all the fields.

2.4. Comparison of H VI and H VII photometry

As can be clearly seen in Figure 1, the H VI and H VII fields contain a significant amount of overlap, allowing me to check the internal consistency of the photometry. The IRAF task *metric*

was used to convert from pixel position on a given chip to RA and Dec coordinates on the sky for all of the stars measured in each field. *Metric* relies upon a solution of the geometric distortion in each field as well as the astrometry information in the image headers. Blind application of the *metric* astrometry resulted in few matches between the two fields. A comparison of the coordinates of individual stars on both fields revealed that there were offsets in RA and Dec between the *metric* astrometry for the two fields even though the scatter was relatively small. The offsets were also a function of which pair of chips each star happened to fall upon and ranged up to an offset of $0.37''$. These offsets were used to correct the *metric* astrometry. A final list of stars detected in both fields was derived using a matching radius of $0.05''$.

If the artificial star tests described in the previous section provide an adequate description of the photometric completeness for each field, then the fraction of stars within the overlap area that are detected in both the H VI and H VII fields should be equal to the product of the completeness fractions in each field. The fraction of stars detected in the H VII field that both lie within the H VI field-of-view and were detected in the H VI field is plotted in Figure 4 as the solid line. The fraction of stars detected in both fields reaches 90% at the bright end and begins to fall rapidly for magnitudes $V > 24$. The dotted line in the figure is the product of the completeness fractions for the H VI and H VII fields derived from the results of the artificial star tests for stars with $0.5 < V - I < 1.5$, the range of color where most of the stars in the CMD are found. The agreement between these two curves indicates that the completeness of the photometry in these two fields is entirely consistent with the artificial star test results.

Plots of the magnitude differences, ΔV and ΔI , divided by the expected error in both V and I , $\sigma_{V,expected}$ and $\sigma_{I,expected}$, for stars in common between the two fields are shown in panels (b) and (d) of Figure 5. The values of $\sigma_{V,expected}$ and $\sigma_{I,expected}$ were defined to be the quadrature sum of the error for each field, shown in panels (a) and (c) of Figure 5 for V and I , respectively. These photometric errors do not include any zeropoint, gain or aperture correction uncertainties and are defined to be the standard deviations of the difference between the input and recovered magnitudes for stars in the artificial star tests. The solid lines in panels (b) and (d) of the figure correspond to zero difference while the dotted lines mark the $\pm 1\sigma$ deviations from zero. While there are stars with magnitude differences between the two fields as large as $4 - 5\sigma$, 83% and 85% of the stars lie within ± 1 standard deviation of zero in the V and I data, respectively. The results plotted in Figure 4 and 5 argue that the artificial star tests provide a reasonable representation of the internal photometric uncertainties and incompleteness in the data.

For the stars measured on both the H VI and H VII fields, an average difference, ΔV and ΔI , and scatter, σ_V and σ_I , for each chip combination was determined by taking the mean difference and standard deviation for stars with $20 < V < 23$ and $19 < I < 22$. These average differences and standard deviations are listed in Table 2. With one exception, the average differences in magnitude agree to within 0.05 mag. With the exception of the WF vs. PC differences, the standard deviations lie in the range $0.07 - 0.09$ and $0.06 - 0.07$ in V and I , respectively. These zeropoint differences are similar to the spread mentioned earlier in the aperture corrections for each field. Assuming that

the relative chip zeropoints and gain ratios as well as the CTE correction were correctly determined by Dolphin (2000b,c), the most likely explanation for the offsets seen between some chips and not others is the uncertainty in the aperture corrections. Furthermore, there are fewer bright stars in the PC chips with which to define the aperture correction, thus making the PC aperture corrections somewhat more uncertain. This may account for the larger differences in the comparison of the PC and WF photometry. Since the H VI and H VII fields are the two most crowded fields in the data, the offsets and uncertainties described here are likely larger than in the other somewhat less crowded fields.

3. Analysis of Field Color-Magnitude Diagrams

Each of the CMDs in Figure 2 shows evidence for stars with a wide range of ages. The plume of stars centered around $V - I$ colors of $0.0 - 0.2$ is the main sequence and contains stars with ages up to about $1 - 2$ Gyr old at the detection limit. Evolved intermediate and high mass stars undergoing core He-fusion with ages up to ~ 1 Gyr are expected to populate a series of “blue loops” in the region between the main sequence and red giant branch. The stellar evolutionary models predict that these stars should spend most of their time at the red and blue ends of the loops, thus producing two sequences in this part of the diagram. In none of the fields are the blue loop sequences very obvious. Each field’s CMD also contains a well-populated red giant branch (RGB) containing somewhat lower mass stars with ages $\gtrsim 1$ Gyr that have left the main sequence but have not yet begun fusing Helium in their cores. After ascending the RGB and undergoing the Helium flash at the RGB tip, stars with ages of approximately $1 - 10$ Gyr end up in the red clump, the strongest feature in each of the observed CMDs. Stars with a wide range of ages all pile up in the red clump since the effective temperature and luminosity are primarily determined by the mass of the He-fusing core, which is approximately constant and independent of the initial main sequence mass (Chiosi et al. 1992). Evolved lower-mass stars fusing Helium in their cores that are $\gtrsim 10$ Gyr old (i.e. stars with main sequence masses $\lesssim 1 M_{\odot}$), would populate a horizontal branch somewhat fainter and bluer of the red clump, as seen for example in the CMD of Carina (Smecker-Hane et al. 1994). However, none of the fields show evidence for a strong horizontal branch although the main sequence and photometric errors at the expected magnitude of the horizontal branch would make it difficult to detect.

While all five CMDs share the same general morphology, there are significant variations among the five fields. The average color of the upper main sequence is bluer in the outer C25 field compared to the more centrally located H IV, H VI and H VII fields, probably indicating differences in the average reddening for each of these fields. In addition, the color spread of the main sequence, even at the brightest magnitudes, appears to be larger in the bar fields compared to the C25 and H VIII fields. As discussed in more detail in §4.4 below, this may indicate some differential reddening in the bar fields. Another difference among the five CMDs is the strength of the main sequence relative to the red giant branch. As a preliminary indicator of the relative ratio of young to old

stars in each of the fields, I determined the ratio of the number of blue ($V - I < 0.75$) to red ($V - I > 0.75$) stars with $V < 23.5$. This limit was chosen because the photometry in all five fields is more than 90% complete down to this magnitude. The ratio of blue to red stars in the the H IV, H VI, H VII, H VIII and C25 fields is 0.52, 0.43, 0.36, 0.34 and 0.15, respectively. These ratios are consistent with a greater recent SFR in the bar compared to the outer regions.

There have been a number of recent studies devoted to the derivation of the SFHs of Local Group galaxies from their CMDs (Mateo 1998). These advances in our understanding of the evolution of nearby galaxies are not only due to better data becoming available but also to improved methods of analyzing the CMDs.

Deriving the ages of star clusters from observed CMDs is relatively simple because the stars in clusters share a common distance, extinction, age and metallicity. In these cases, simply overplotting theoretical isochrones of the appropriate metallicity on the observed CMD is sufficient to determine the age. The observed CMDs of field stars in galaxies, such as those for NGC 6822 presented in the preceding section, are much more complicated and represent a superposition of stars with a variety of ages and metallicities. In some parts of the diagram, stars with different ages and metallicities have similar colors and magnitudes, making simple isochrone fitting inadequate to derive the ages of the stars. Recently, there have been a number of methods proposed to extract quantitatively the star formation history of a galaxy based upon CMDs of its stars (Marconi et al. 1995; Gallart et al. 1996a,b; Tolstoy & Saha 1996; Dolphin 1997; Dohm-Palmer et al. 1997; Hurley-Keller et al. 1998; Olsen 1999; Holtzman et al. 1999; Hernandez et al. 1999). All of these methods construct a series of model CMDs using a set of theoretical isochrones and the results of artificial star tests. These methods differ in many of the details such as which parameters (i.e. distance, extinction, metal enrichment, etc.) are assumed and which are extracted from the CMD fit. Furthermore, these different authors choose different statistical methods for comparing the models and observations as well as the criteria by which the best-fitting model is determined.

In the remainder of this section, I describe three of these methods that I have used to derive the field star formation history in the five *HST* WFPC2 fields analyzed here. The method whose results I will rely most heavily upon is that developed by Dolphin (1997) and described below in §3.1. This method differs from the other two described in this section in that it attempts to fit the entire CMD all at once instead of focusing on certain phases of stellar evolution. Furthermore, it is able to simultaneously solve for the star formation rate while accounting for uncertainties in other parameters, such as the extinction and metallicity.

The motivation for choosing two other analysis methods was in part to provide a check on the results from the more automated Dolphin (1997) approach and also to investigate the different SFH conclusions derived from three separate analyses. Given the many different SFH analysis methods that have been applied to different galaxies, it would be interesting to establish whether different methods, when applied to the same data, yield the same result. An additional motivation for choosing the Gallart et al. (1996a) method was to determine whether the results Gallart et al.

(1996a) derived from ground-based data of NGC 6822 could be recovered from the new *HST* data presented here.

In contrast to the Dolphin (1997) method, the methods developed by Gallart et al. (1996a) derive information about the SFH by comparing the distribution of stars in the red giant branch to a series of model CMDs constructed from a predetermined set of SFHs. By concentrating solely on the red giant branch, this method is only able to infer information about the SFH for ages greater than about 1 Gyr. This method is inherently somewhat more limited than the Dolphin (1997) method because it is only possible to compare a more limited set of SFH models with the observed CMD as described below in §3.2 in more detail. The Gallart et al. (1996a) method has the advantage that it provides easier insight into why certain models provide a better fit compared to others. Since the Gallart et al. (1996a) method only provides information about the intermediate age and old SFH, the main sequence luminosity function was also used to infer the recent SFH, as proposed by Dohm-Palmer et al. (1997). The results of these three analyses are presented in §4.

Throughout the remainder of this paper, the PC photometry is excluded from the analysis. The CMDs of the star clusters appearing in the PC have already been presented and analyzed in Wyder et al. (2000).

3.1. Derivation of the Star Formation History using the Dolphin (1997) Method

In this section, I present an analysis of the SFH of NGC 6822 based upon the methods developed by Dolphin (1997, 1999) who has kindly provided many of the computer programs used for the following analysis.

3.1.1. Model Ingredients

The theoretical stellar evolutionary isochrones used here to construct model CMDs are those calculated by the Padova group (Bertelli et al. 1994; Girardi et al. 2000, and the references in both papers). Both sets of models follow the evolution of stars from the zero age main sequence all the way through to carbon ignition in higher mass stars and to the thermally pulsing asymptotic giant branch phase in lower mass stars. They include the most recent opacities and equations of state as well as some amount of convective overshoot and semi-convection in stars with convective cores. The programs used here rely mostly on the more recent Girardi et al. (2000) models which describe the evolution of stars with masses from 0.15 to $7 M_{\odot}$ for metallicities from $Z = 0.0004$ to $Z = 0.03$. For stars with masses in excess of $7 M_{\odot}$, these results are supplemented with the Bertelli et al. (1994) models while the Girardi et al. (1996) data for $Z = 0.0001$ are used to extend the set of isochrones to very low metallicities. The tracks for stars between 5 and $7 M_{\odot}$ are very similar between the new and old sets of isochrones (Girardi et al. 2000), so no shift was needed to match the old and new models. The effects of the newer isochrones on the interpretation of stars along the

red giant branch could potentially be larger. However, the similarity between the results derived below in the present work using a combination of the new and old Padua isochrones and those from Gallart et al. (1996a), who relied entirely upon the old set of models, argues that adopting one isochrone set over the other does not lead to wildly different results. In all of these models, the theoretical luminosities and effective temperatures were converted into observable *UBVRI* magnitudes by Bertelli et al. (1994) and Girardi et al. (2000) using the convolution of the filter response curves with the Kurucz (1992) model stellar atmospheres. The theoretical isochrones are tabulated for discrete ages and metallicities. In order to create stars with arbitrary metallicities and ages, the isochrones must be interpolated to any desired age and metallicity using a set of equivalent evolutionary points along each isochrone.

In order to populate the isochrones with stars, I have assumed a power law initial mass function of the form

$$\phi(\log m)d\log m = \phi_0 m^{-\alpha} d\log m \quad (1)$$

where m is measured in M_\odot . I have assumed a constant value of the IMF exponent of $\alpha = 1.35$. The IMF is assumed to extend from $120 M_\odot$ down to $0.1 M_\odot$. This leads to an average mass of $0.352 M_\odot$ and normalization of $\phi_0 = 0.06$.

In addition to the IMF, an extinction, reddening and distance must be assumed in order to compare the models and observations. In the SFH fits described below, the extinction A_V is allowed to vary while the corresponding value of $E(V - I)$ is calculated assuming the Galactic reddening law from O'Donnell (1994) with $R_V = A_V/E(B - V) = 3.1$, as tabulated for different filter systems in Schlegel et al. (1998). This leads to the relation $E(V - I)/A_V = 0.419$. The ratio of $E(U - B)/E(B - V) = 0.74 \pm 0.07$ measured by Massey et al. (1995) for NGC 6822 is consistent with the Galactic reddening law and supports this assumption. Each field is assumed to have a single value of A_V appropriate for all of the stars in the CMD.

Another ingredient in generating model CMDs is the chemical enrichment law (CEL). For each model CMD, the metallicity is assumed to increase from some initial metallicity Z_i to a final metallicity Z_f following one of three chemical enrichment laws which are shown in Figure 6 for $Z_i = 0.0001$ ([Fe/H] = -2.3) and $Z_f = 0.004$ ([Fe/H] = -0.7). As discussed in more detail below, models assuming various combinations of Z_i , Z_f and enrichment law were created and used to solve for the SFH. These metal-enrichment laws are not motivated by any specific physical model but rather were chosen to span a reasonable range of possible metallicities in each time bin. A single value for the metallicity is assumed for each age.

3.1.2. Description of the Method

For a detailed description of this method, see Dolphin (1997) and Dolphin (1999). A brief overview is given in this section.

The model CMDs are constructed using the following steps. The number of stars in the model CMDs is stored in a series of color and magnitude bins in the CMD. The number of stars in each bin of the model CMD will then be fit to the observed number in each bin to determine the best-fitting SFH. A series of time bins is also chosen for the solution with the duration of the bins generally increasing with age to account for the fact that isochrones for older stars tend to bunch more closely together in the CMD than the isochrones for younger stars.

Assuming some combination of values for the extinction, metal enrichment law, initial and final metallicities, distance and IMF, a series of model "basis" CMDs are created by assuming a constant SFR of $1 M_{\odot} \text{ yr}^{-1}$ for the duration of each time bin and none at other times. A set of interpolated isochrones is then calculated with spacing in age much smaller than the duration of the bin. These isochrones along with the assumed IMF are then used to determine the number of stars formed in each CMD color-magnitude bin for this particular time bin. The metallicity is assumed to increase linearly from the beginning to the end of the time bin with the initial and final values derived from the assumed chemical enrichment law. For each isochrone point, the artificial star test results are used to determine in which CMD bins a star with that particular intrinsic color and magnitude could have been observed. The result of this procedure is a series of model CMDs for the assumed set of input parameters that show how stars within each time bin are distributed within the diagram for a SFR of $1 M_{\odot} \text{ yr}^{-1}$. As an illustration of this procedure, I have created a model CMD using the artificial star test results for the H VIII field assuming a constant SFR of $5 \times 10^{-4} M_{\odot} \text{ yr}^{-1}$ from 15 Gyr ago to the present, an initial and final metallicity of $[\text{Fe}/\text{H}] = -2.3$ and -0.7 , respectively, and the second enrichment law shown in Figure 6. The resulting model CMDs for each age bin are shown in Figure 7. As is evident from the figure, stars older than about 1 Gyr are concentrated in the red clump (RC) and red giant branch (RGB) while stars younger than a Gyr lie along the main sequence and blue loops between the RGB and main sequence.

The choice of the time bins shown in Figure 7 is somewhat arbitrary. Ideally, one would like to chose the time bins such that each of the basis CMDs is significantly different from one-another to avoid degeneracies in the fitting while at the same time being able to reproduce the full range of possible SFHs. While such an investigation is beyond the scope of this paper, it is possible to test whether the time bins shown here significantly bias the SFH solutions derived. To test this, I have solved for the SFH in the H VIII field using the fitting procedure and assumptions described below using three different choices for the time bins. For the first test, 12 time bins were selected from 10 Myr to 15 Gyr, varying in length from 0.2 Gyr for the youngest ages to 2 Gyr for the oldest bin. For the second and third tests, the time bins were chosen with duration $\Delta \log(t) = 0.1$ and $\Delta \log(t) = 0.2$, respectively, between 10 Myr and 15 Gyr. In all three tests, the solutions were determined using the assumptions about the metallicity, extinction, distance, etc. described below. The resulting SFRs vs. time are plotted in Figure 8. The three panels in the first column show the solutions at their full resolution while the second column shows the same solutions rebinned to match as closely as possible the time bins used for the final results presented below in §4. Despite the varying number of time bins in each solution, the resulting SFRs, when binned to the same

resolution are similar to within the errors.

The object of the fitting procedure is then to determine which linear combination of these single time bin CMDs best represents the data. More specifically, the number of model stars present in the i th color-magnitude bin of the CMD, N_i , is given by

$$N_i = \sum_j c_j M_{ij} \quad (2)$$

where c_j is the coefficient for the j th time bin and M_{ij} is the number of stars in the i th CMD bin of the j th time bin assuming a SFR of $1 M_\odot \text{ yr}^{-1}$. Thus, the c_j coefficients are the SFRs (in units of $M_\odot \text{ yr}^{-1}$) for each time interval.

In order to determine the SFH that best represents the data, a parameter is needed to describe how well a model fits the data. Ideally, one would want to use a χ^2 statistic for the comparison. However, in practice bad points in the CMD, foreground stars and other objects which contaminate the CMD bias such a statistic making it difficult to derive a good fit. In addition there are certain evolutionary phases, particularly the blue loops and red clump where the models are more uncertain. To avoid having the fitting statistic being biased towards areas of the CMD where there are observed stars but few or no model stars, a modified χ^2 statistic was adopted which I will denote as $\bar{\chi}^2$. It is given by

$$\bar{\chi}^2 = \sum_i \frac{(N_i - n_i)^2}{N_i} \quad (3)$$

where n_i is the number of observed stars in the i th CMD bin and N_i is the number of model stars. In order to account for poorly fit stars as well as some amount of foreground contamination, a term xLF is added to the value of N_i in each bin, where LF is the number of model stars in that interval of magnitude, regardless of color, and x varies linearly from 0.1 at the bright end of the CMD to 0.4 at the faint end. In addition, if in any particular bin $\bar{\chi}_i^2 > 9$, then the value for that bin is replaced by the value of $(6\bar{\chi}_i - 9)$ so that the value of $\bar{\chi}^2$ does not blow up so quickly for large differences between the model and data. This particular modification was chosen such that both $\bar{\chi}^2$ and its derivative are continuous. The set of SFR coefficients producing the minimum value of $\bar{\chi}^2$ is then the best-fitting solution. Unfortunately, given the modifications to the fit parameter from a traditional χ^2 , it is difficult to quantify the significance of the solutions. A detailed investigation of the statistical significance of an individual SFH solution is beyond the scope of the present work. Nevertheless, the value of $\bar{\chi}^2$ should rank the solutions in a relative sense.

The above discussion of fitting the observed CMD describes a solution in which only the SFR(t) was allowed to vary while all of the other input parameters (extinction, metal enrichment law, initial metallicity, final metallicity, IMF, distance) were assumed constant. Given good enough photometry, the effects of these parameters on the CMD are different enough so that each of these parameters can be allowed to vary and solved for as a parameter in the fit (Dolphin 1997). In such a case, the procedure described above is repeated many times with each of the parameters allowed to vary within some specified range. Then some number of the best-fitting solutions are chosen. A

weighted average of these solutions then provides estimates of all of the input parameters as well as the SFH. Furthermore, the spread in the SFRs and the other parameters can be used as an estimate of their probable errors. The data presented here do not go far enough down the main sequence to make such a full solution possible. Since some of these parameters are fairly well constrained by other observations of NGC 6822, I have only allowed some of these parameters to vary while fixing others.

A summary of the parameters that I have fixed as well as the ranges tried for other parameters is shown in Table 3. As discussed in the introduction, the distance to NGC 6822 is fairly well-established. In all of the fits, I have assumed the Cepheid distance modulus of $(m - M)_0 = 23.49$ as derived by Gallart et al. (1996c). The extinction A_V was allowed to vary from 0.6 to 1.3 mag in steps of 0.1, thus bracketing the range of extinctions (including both foreground and internal) that have been estimated for NGC 6822 in the past (Massey et al. 1995).

The current oxygen abundance in the gas of NGC 6822 is substantially less than solar, as first shown by Peimbert & Spinrad (1970). Pagel et al. (1980) measured the oxygen abundances for seven H II regions and found an average abundance of $12 + \log(O/H) = 8.25 \pm 0.07$ which corresponds to $[\text{Fe}/\text{H}] = -0.7$ for a solar O/Fe ratio. Confirming these results, Skillman et al. (1989b) determined an abundance for the H II region H V of $12 + \log(O/H) = 8.20$. In contrast to those studies, the average abundance of the six H II regions observed by Chandar et al. (2000) is $12 + \log(O/H) = 7.91 \pm 0.06$, corresponding to an overall metallicity of $[\text{Fe}/\text{H}] = -1.0$. Unfortunately, there are no H II regions in common between the Chandar et al. (2000) and Pagel et al. (1980) samples, so it remains unclear whether the different results represent a real abundance spread or whether there is some zeropoint difference between the two studies. In addition to the H II regions, abundances for individual high mass stars in NGC 6822 are beginning to be determined. Based upon high resolution spectroscopy, Venn et al. (2001) determined the oxygen abundance for two A-type supergiants to be similar to the Pagel et al. (1980) results. The mean oxygen abundance for these two stars is $12 + \log(O/H) = 8.36 \pm 0.19 (\pm 0.21)$ where the two uncertainties correspond to random and systematic errors, respectively. Furthermore, the iron lines in the stellar spectra lead to a solar O/Fe ratio: $[\text{O}/\text{Fe}] = +0.02 \pm 0.20 (\pm 0.21)$. These values stand in contrast to observations of Galactic low metallicity stars which show an overabundance of oxygen relative to other heavy elements (Wheeler et al. 1989). The Venn et al. (2001) results are consistent with spectra of two B-type supergiants that have an average metallicity of $[\text{Fe}/\text{H}] = -0.5 \pm 0.2$ (Muschielok et al. 1999). The different metallicities determined from these various studies could indicate a possible spread in the current metallicity of NGC 6822 although no trend with galactocentric distance is yet obvious. Due to these lingering uncertainties, I have allowed the current metallicity to vary from $[\text{Fe}/\text{H}]_f = -0.7$ to -1.1 in steps of 0.2 dex.

The only observational constraints on the initial metallicity in NGC 6822 that are independent of the distribution of stars on the RGB come from observations of the cluster H VII. Based upon its integrated spectrum, Cohen & Blakeslee (1998) derived a metallicity of $[\text{Fe}/\text{H}] = -1.95 \pm 0.15$ dex and age of 11_{-3}^{+4} Gyr. These results are in general agreement with the age of (10 ± 2) Gyr

and metallicity of $[\text{Fe}/\text{H}] \sim -2.0$ determined by Chandar et al. (2000). The CMD and structure of H VII from the *HST* data also support the conclusion that H VII is likely similar to Milky Way globular clusters (Wyder et al. 2000). The initial metallicity for the SFH solutions was chosen to bracket the H VII metallicity and was allowed to vary from $[\text{Fe}/\text{H}]_i = -2.3$, the lowest value available from the stellar evolutionary models, to $[\text{Fe}/\text{H}]_i = -1.4$ in steps of 0.3 dex.

When fitting their ground-based CMDs of NGC 6822, Gallart et al. (1996a) found that a common feature of accepted models was that stars in the 6 – 9 Gyr age range have metallicities of $Z \approx 0.002 - 0.003$, or $[\text{Fe}/\text{H}] \approx -0.9$. The accepted models either had star formation beginning 12-15 Gyr ago at a low metallicity ($Z_i = 0.0001$) or star formation beginning 6 – 9 Gyr ago from gas at a somewhat higher metallicity ($Z_i = 0.002$). In all of their models a metal enrichment law linear in Z was assumed leading to a metallicity of $Z = 0.002 - 0.003$ for stars formed 6 – 9 Gyr ago. This metallicity for 6 – 9 Gyr-old stars is roughly consistent with the first two chemical enrichment laws shown in Figure 6, regardless of the initial or final metallicity. However, it is inconsistent with the chemical enrichment law that is linear in $[\text{Fe}/\text{H}]$ for low initial metallicities. As is shown in the next section, these models tend to provide a worse fit to the data than the other enrichment laws.

With these choices of parameters, all of the SFH solutions were performed using the following steps. For each solution the chemical enrichment history was fixed by choosing one of the possible combinations of $[\text{Fe}/\text{H}]_i$ and $[\text{Fe}/\text{H}]_f$ as well as one of the three enrichment laws shown in Figure 6. Then a solution was determined for a series of values of A_V , beginning with $A_V = 0.9$. Next the value of A_V was increased or decreased in steps of 0.1 mag until the minimum of the fit parameter $\bar{\chi}^2$ was found. The value of A_V was constrained to lie within the range specified in Table 3. This was repeated for each combination of $[\text{Fe}/\text{H}]_i$, $[\text{Fe}/\text{H}]_f$ and chemical enrichment law. The final values of the SFR and metallicity for each time bin and the best-fitting value of A_V were determined by averaging together some number of the best-fitting solutions. The spread in each of the parameters as well as the SFRs in each bin among the best solutions provides an estimate of the likely uncertainties in each of the parameters.

3.2. Derivation of the Star Formation History using the Gallart et al. (1996a) Method

A somewhat different approach in deriving the SFH has been used by other authors. These approaches have in common that they concentrate on certain specific regions of the CMD for comparison of model diagrams with the observed data. Although such an approach has the limitation that it does not make use of all of the information in the CMD, it does have the advantage of allowing a better understanding of why certain models provide a better fit compared to others. In this section, I attempt to duplicate the methods used by Gallart et al. (1996a) to derive the SFH for the old and intermediate age stars for the H VIII field.

3.2.1. Model Ingredients

Many of the ingredients used to construct the models used in §3.1 are also used here. The evolutionary models are the same combination of the Girardi et al. (2000) and Bertelli et al. (1994) results described above. The distance and IMF are identical to those assumed already as well. For the H VIII field, I have assumed an extinction of $A_V = 0.82 \pm 0.1$, the value determined by the full SFH solutions via the Dolphin (1997) method. (See §4.2).

The same series of SFH shapes adopted by Gallart et al. (1996a) were assumed here and are shown in Figure 9. The main goal of adopting these shapes is to determine the overall trend in the SFR with time. For each SFH shape, three equal length time bins are assumed from the time of initial star formation T_i to the present. In practice, the recent star formation is truncated at 10 Myr. The SFR is allowed to change amplitude once, either at $1/3T_i$ or at $2/3T_i$. The higher SFR is assumed always to be four times the lower SFR. In addition, a constant SFR case is considered. All five shapes are normalized to the same integrated mass of stars formed. The SFH shapes have been ordered such that they progress from a predominantly young population in Shape 1 to a predominantly older population in Shape 5. Shape 3 is the constant SFR case. Four values of T_i have been considered: 15, 12, 9 and 6 Gyr.

The same metal enrichment law assumed by Gallart et al. (1996b) is assumed here. The metallicity is assumed to increase linearly in Z from its initial value $Z_i = 0.0001$ ([Fe/H] = -2.3) to the current metallicity of $Z_f = 0.004$ ([Fe/H] = -0.7). Models with the same final metallicity but with $Z_i = 0.002$ were also generated.

For each value of T_i , a synthetic CMD was produced assuming a constant star formation rate in the three time bins of $5 \times 10^{-3} M_\odot \text{ yr}^{-1}$, a rate about 10 times that in the observed H VIII CMD. Thus, many more model stars are created than observed stars to reduce the noise in the model CMD. Then the number of stars created in each time bin was scaled relative to one another to create model CMDs for each of the five SFH shapes. The observational errors and incompleteness were incorporated in the models using the results of the artificial star tests. There are therefore a total of 40 model CMDs given all the possible combinations of the four values of T_i , the five SFH shapes and the two values of Z_i .

3.2.2. Definition of Indicators Relative to the Red Giant Branch

In order to compare their model and observed CMDs, Gallart et al. (1996a) calculated several indicators relative to the distribution of stars in the “red tangle,” a region containing the RGB, and the “red tail,” the region of the CMD above and redward of the RGB consisting primarily of asymptotic giant branch (AGB) stars. In particular the color distribution of stars in the red tangle in the magnitude interval $-3.75 < M_I < -3.25$ was used to discriminate among the different models.

The CMDs analyzed here do contain a few stars brighter than the RGB which are likely part of the red tail structure seen in the ground-based CMDs. It is difficult to use these stars to place constraints on the SFH due to their small numbers. In addition, the saturation limit in the *HST* data occurs at $I \approx 19$, a level only about 1 mag above the TRGB. Thus, I have chosen to use the distribution of stars along the RGB and RC to differentiate between the different models. The definitions of the regions in the CMD used for the analysis are shown in Figure 10 superposed on the $M_I, (V - I)_0$ CMD for the H VIII field. There are four regions along the RGB as well as a region containing the RC. The brightest RGB region was chosen to be nearly identical to the region of the red tangle used by Gallart et al. (1996a). Similar to the AGB, the RC contains intermediate age stars 1 – 10 Gyr old. However, it is less sensitive to age and metallicity as shown below in §4.

For each of the 40 model CMDs, the average SFR was calculated by scaling the number of model stars in the four RGB regions to match the observations. This was accomplished by minimizing the χ^2 statistic given by

$$\chi^2 = \sum_{i=1}^4 \frac{(N_i - n_i)^2}{N_i} \quad (4)$$

where N_i is the number of model stars in the RGB bin and n_i is the number of observed stars in the same bin.

For each combination of T_i , SFH shape and Z_i the color distribution of stars in the brightest RGB region was calculated, scaled to the observations using the average SFR for that model. A grid of the resulting model color distributions for the brightest RGB region are shown as the solid lines in Figure 11 for the $Z_i = 0.0001$ case. The observed color distribution is plotted in each panel as the dotted line. Each row of the figure corresponds to a SFH shape which is labeled in the corner of every panel while each column corresponds to the value of T_i labeled at the top. It is clear that the models with star formation beginning as soon as 6 or 9 Gyr ago tend to produce RGBs that lie blueward of the observed RGB. For each value of T_i , a secondary blue peak in the RGB color distributions for SFH shapes 1, 2 and 3 appears. The peak becomes more prominent relative to the red peak as the proportion of young stars increases. The stars in the blue peak are intermediate mass evolved stars with ages < 1 Gyr that lie along the red end of the blue loops in the CMD. The lack of this secondary peak in the observed CMD argues against a SFH with most of the star formation occurring within the most recent third of the galaxy’s history.

To better quantify the differences between the model and observed color distributions, I have defined three indicators all of which were used by Gallart et al. (1996a) in their analysis. The first is the median $V - I$ color of the RGB. The second indicator is C95 which marks the red edge of the RGB. It is calculated by finding the color below which 95% of the stars lie. The third is a χ^2 statistic similar to that shown in equation 4 except that now the summation is made over bins in color. I have restricted the calculation to only include those color bins where the number of model stars is non-zero and the number of observed stars is greater than six. The latter limit was chosen to insure that the results are not dominated by the bins with few stars.

In addition to the color distribution of stars in the RGB, I have calculated for each model the ratio of stars in the RC region to the number stars in each of the RGB regions. When stars reach the RC and begin core He fusion, the mass of the He-burning core is similar for stars with a wide range of initial masses (Chiosi et al. 1992). This means that the amount of time a star spends in the RC is relatively insensitive to its original main sequence mass. On the other hand, the time it takes for a star to ascend the RGB does tend to increase with decreasing mass (Chiosi et al. 1992). As a consequence, one would expect the ratio of RGB stars to RC stars to increase with the dominant age of the stellar population. For a more detailed discussion concerning the use of this ratio in constraining the SFHs of Local Group dwarf galaxies see Tolstoy et al. (1998) and Cole et al. (1999).

3.3. The Recent Star Formation History from the Main Sequence Luminosity Function

While the old and intermediate age stars are concentrated in the RGB and RC structures in the CMD, the younger stars with ages less than about 1 Gyr, are distributed along the main sequence (MS) and He-burning blue loops. Along these sequences, stars of similar masses have similar brightnesses, a fact which can be exploited to determine the recent SFH from the luminosity functions of stars in these two parts of the diagram. Dohm-Palmer et al. (1997) developed a method to derive the SFH from the MS luminosity function which I have applied here to all five *HST* fields in NGC 6822.

Although stars have similar masses for each magnitude along the main sequence, they can have any age less than or equal to the MS turn-off age for that mass. The Dohm-Palmer et al. (1997) method relies on the following equation for the number of stars $C_n(M_V)$ within the n th magnitude bin of the MS luminosity function:

$$C_n(M_V) = \int_{m_1}^{m_2} \phi(m) dm \sum_{i=1}^n \frac{R_i}{\langle m \rangle} \Delta t_i \quad (5)$$

where R_i is the SFR in the i th bin in units of $M_\odot \text{ yr}^{-1}$, $\langle m \rangle$ is the average mass (in M_\odot) weighted by the IMF and Δt_i is the difference in turnoff age between the beginning and end of the magnitude bin. ϕ is the IMF defined by equation 1, with the same exponent and normalization as used for the automated fits of the CMD. Finally, m_1 and m_2 are the corresponding MS turnoff masses at the faint and bright ends of the magnitude bin, respectively. These equations can be solved for the values of R_n by taking the difference between neighboring bins with the convention that n increases with magnitude. Thus the value of the SFR corresponding to the n th magnitude bin is given by

$$R_n = \frac{\langle m \rangle}{\Delta t_n} \left(\frac{C_n}{A_n} - \frac{C_{n-1}}{A_{n-1}} \right) \quad (6)$$

where A_n is the integral over the IMF between the minimum and maximum turnoff masses for

the n th magnitude interval. The minimum V magnitude in each CMD was limited to 20 due to saturation. The SFR corresponding to brighter magnitudes was set to zero.

To apply these equations to the data the MS turnoff age and the MS turnoff mass are needed as a function of M_V . These relations were taken from the Bertelli et al. (1994) stellar models. For each field the model data were interpolated to the endpoints of each of the magnitude bins used to construct the main sequence luminosity function. The conversion between absolute and apparent magnitude was calculated assuming a distance modulus of 23.49 and the extinctions listed in Table 6 which were derived using the methods presented in §3.1.

The curve used to define the main sequence is shown in Figure 10 as the dashed line superposed on the H VIII CMD. The main sequence stars were defined to be all stars that lie blueward of this line. For the other fields, the curve was shifted according to the appropriate reddening for each field. The observed MS luminosity function was then calculated for each field using 0.5 mag wide bins down to a limiting apparent magnitude of $V = 25.5$ where the completeness in all five fields is greater than 30%. A set of artificial stars with input $V - I$ colors greater than 0.0 and less than the same curve used to define the observed MS was chosen to determine the completeness as a function of magnitude for the MS. Finally, the recent SFHs for each field were calculated from the completeness corrected luminosity functions using equation 6. The errors in each of the SFRs were determined from the errors in the completeness corrections as well as the Poisson errors in the number of observed stars in each bin. The Poisson errors dominate the total error in the SFR for each bin.

Before proceeding with presenting the results, it is important to emphasize some of the limitations common to all three methods presented in this section. First, there is undoubtedly some fraction of unresolved binary stars in the CMDs whereas the SFH solutions used here assume that it is zero. Second, there could be some intrinsic spread in metallicity at a given age which the solutions given here assume is zero. Third, I have neglected any differential reddening within each field. Fourth, I have assumed a single power law IMF with exponent equal to the original value determined by Salpeter (1955). While there is some evidence that the form of the IMF does not vary widely with environment, measurements of the IMF are uncertain enough that significant variations with time or among different galaxies can not be ruled out (e.g. Kennicutt 1998b). Finally, and probably most importantly, these solutions ignore any possible systematic errors and uncertainties in the stellar evolutionary models. As was noted by Holtzman et al. (1999), all of the derivations of the SFHs of Local Group galaxies produce model CMDs which are statistically incompatible with the observations. This is likely a result of the many approximations used in deriving the best-fitting SFH but is also likely in part due to the uncertainty in the stellar models.

4. Results and Discussion

In the previous section, I have described the different methods utilized to infer information about the star formation history of NGC 6822 from the observed CMDs. In this section, the results of these analyses are presented.

4.1. Age of the Oldest Stars

One of the most basic questions we would like to know about galaxies is when their first stars began forming. The cluster H VII has a likely age of 11^{+4}_{-3} Gyr, indicating that star formation began at least about 8 Gyr ago (Cohen & Blakeslee 1998). On the other hand, Gallart et al. (1996a) concluded that star formation in NGC 6822 most likely began about 15 Gyr ago based upon their ground-based CMDs. They also showed that the CMD could also be consistent with star formation beginning as soon as 6 Gyr ago if there were prompt metal enrichment at the onset of star formation to half its current value. The metallicity of H VII measured by Cohen & Blakeslee (1998) would argue against this possibility although it is possible that H VII and the field stars formed during the same period may not have shared the same metallicity.

Using the techniques developed by Dolphin (1997) and outlined in §3.1, I have explored to what extent the *HST* data can be used to place constraints on the time when star formation began in NGC 6822. For this experiment, I have concentrated on the H VIII field due to its somewhat lower crowding than the other Hubble cluster fields. Using the parameters listed in Table 3, I have solved for the SFH in this field under three different assumptions about the ages of the oldest stars, T_i . In each solution, the same eight time bins were used except for the beginning of the oldest time bin. I have chosen to perform the solutions for $T_i = 15, 12$ and 9 Gyr.

The results for a subset of the solutions are plotted in Figure 12 for an assumed extinction of $A_V = 0.8$. Each panel of the figure plots the value of the fit parameter $\bar{\chi}^2$ as a function of T_i for a particular combination of $[\text{Fe}/\text{H}]_i$ and $[\text{Fe}/\text{H}]_f$. The solid, dotted and dashed lines in each panel correspond to the enrichment laws 1, 2 and 3, respectively, as plotted in Figure 6. For clarity only the solutions for the extreme values of $[\text{Fe}/\text{H}]_i$ are shown here.

While in general the value of the fit parameter decreases with increasing T_i for a given chemical enrichment history, this conclusion depends sensitively on the assumptions made about the metal enrichment history. For a given value of the initial metallicity, increasing the final metallicity tends to decrease the differences in fit parameter among the three values of T_i . This somewhat counterintuitive result is due to the fact that changing the value of $[\text{Fe}/\text{H}]_f$, while holding the enrichment law and $[\text{Fe}/\text{H}]_i$ constant, increases the spread in metallicity in the oldest time bin, thus allowing the CMD to be fit equally well by a SFH with a smaller range in age. The chemical enrichment law 1, the chemical enrichment law with the most rapid increase in metallicity with time, results in the best fit for a specific choice of initial and final metallicity, particularly for low

values of the initial metallicity. Increasing the initial metallicity tends to decrease the differences in fit parameter among the three different enrichment laws because decreasing the difference in initial and final metallicities tends to make the chemical enrichment histories derived from the three chemical enrichment laws more similar to one another.

For each value of T_i , an average SFH and metal enrichment history was derived by averaging together the approximate 30 best solutions. The results are summarized in Table 4 which lists the minimum fit parameter found for each choice of T_i as well as the maximum fit parameter used to select the best solutions. The third column lists the resulting number of solutions averaged. The derived value of A_V appears to increase as T_i decreases although the difference is small. While one should keep in mind the systematic trends with metallicity shown in Figure 12, overall the fits tend to worsen as T_i decreases. Table 5 lists the SFRs as a function of age for each value of T_i while Figure 13 plots the SFRs and metallicities. As is evident from the tables, the star formation rate for ages up to 3 Gyr is relatively unaffected by the choice of T_i . For older ages, however, the SFR in the oldest time bin increases as T_i decreases. Furthermore, the star formation rate in the 5 – 7 Gyr bin decreases with T_i while the star formation rate in the 3 – 5 Gyr bin increases.

The best-fitting average SFRs and metallicities plotted in Figure 13 were used to construct model CMDs which are shown in Figure 14 for each value of T_i along with the observed CMD. As would be expected, the main difference in the morphology of the CMD is the distribution of stars along the RGB. As T_i decreases, the RGB tends to become narrower. As is well known, there is an age-metallicity degeneracy for RGB stars in that a blue RGB can be produced by either an old, metal-poor population or by a younger and more metal-rich one. On the other hand, the width of the RGB could be increased somewhat if a spread in metallicity at each age were allowed.

The results of the analysis using the Gallart et al. (1996a) methods, as described in §3.2, point toward a similar conclusion regarding the age of the oldest stars in NGC 6822. Plots of the median color, C95 color and $1/\chi^2$ as a function of SFH shape are shown in Figure 15 for the brightest RGB region 1. The solid lines in each plot show the observed value and, in the case of the median and C95 colors, the $\pm 1\sigma$ error bars, calculated assuming a ± 0.05 uncertainty in the reddening. While the median and C95 colors are rather insensitive to the SFH shape, they are able to discriminate between different values of T_i . Consistent with expectations, the RGB tends to become bluer as the time of initial star formation decreases. The differences among the different models are largest for the brightest RGB bin and become more similar to each other for the fainter bins. Thus only the results for the brightest bin are considered here. The only model whose indicators are all consistent with the observed values is the $T_i = 15$ Gyr case with the $T_i = 12$ Gyr model being just barely excluded by the C95 indicator. This same conclusion is supported by the values of $1/\chi^2$. The models with star formation beginning 12–15 Gyr ago and SFH shapes 3 and 4 provide the best fits. It is important to bear in mind that these conclusions rest on the assumption of a low initial metallicity. Similar fits were attempted for an initial metallicity of $[\text{Fe}/\text{H}] = -1.0$ and the results are plotted in Figure 16. For this higher metallicity, the median and C95 colors are consistent with values of T_i from 6 – 12 Gyr and show a slight preference for SFH shapes 1 and 2. The value of

$1/\chi^2$ for all the models is less sensitive to the SFH shape and do not reach as high values as for the low metallicity case. These results are entirely consistent with the conclusions reached by Gallart et al. (1996a) based on the same analysis of their ground-based CMDs in that the distribution of stars near the tip of the RGB can be fit by star formation beginning at younger ages if the initial metallicity is high.

In Figure 15(c), the ratio of the number of stars in RGB region 1 to the number of stars in the RC is shown as a function of SFH shape. The model ratios are very similar for all values of T_i and are not able to reproduce the observed ratio. For the models plotted in 15(c), there is a small increase in the ratio from SFH shapes 1 to 5, consistent with the rising fraction of older stars from Shapes 1 to 5. The origin of the difference is not obvious and may be due to some combination of uncertainties in the stellar models, the limited set of SFH solutions attempted here or possibly a non-Salpeter IMF. In particular, the He-burning lifetimes of stars in the RC depend strongly upon the assumptions made concerning convective overshoot which may lead to systematic uncertainties in the stellar models (e.g. Bertelli & Nasi 2001). The same discrepancy is apparent in the high initial metallicity fits in Figure 16. Although not plotted in these figures, the RGB to RC ratio in the models is lower than the observations for each of the RGB regions shown in Figure 10 individually. Thus, the discrepancy would not be solved by including stars further down the RGB in the calculation.

In summary, both the Dolphin (1997) and Gallart et al. (1996a) analysis are best able to fit the observed CMD with star formation beginning 15 Gyr ago. However, it is important to emphasize that depending upon the assumptions made about the metal enrichment history, the CMDs can also be fit by star formation beginning at younger ages. In particular, the trends in Figure 12 show that the observed CMD of NGC 6822 can be fit equally well by star formation beginning only 9 Gyr ago, even for low initial metallicities, if the metallicity increase with time is rapid. This is similar to the conclusion reached by Gallart et al. (1996a) that assuming a high initial metallicity allows the RGB to be fit by younger ages. More definitive conclusions about when NGC 6822 began forming stars must await either deeper CMDs or independent information about the abundances of stars along the RGB.

One of the hallmarks of a truly old, globular-cluster age population ($\gtrsim 10$ Gyr old) is the presence of a horizontal branch. None of the CMDs presented in the preceding chapter show any evidence for a strong horizontal branch, which would be expected somewhat fainter and blueward of the red clump as seen, for example, in the CMD of Carina (Smecker-Hane et al. 1994). Still, the photometric errors at the expected level of the horizontal branch around $V \approx 25$ as well as the strong main sequence may be masking any horizontal branch, if present. No searches for RR Lyrae variables, which are readily identifiable horizontal branch stars, have yet been published for NGC 6822.

4.2. Old and Intermediate Age Star Formation Histories for all Five Fields

The SFHs for the five *HST* fields were derived using the Dolphin (1997) method with the parameters listed in Table 3 and the same time bins as for the H VIII solutions already presented. As $T_i = 15$ Gyr provides the best fit to the H VIII data, I have adopted this value for all of the fields. Before discussing the results for each of the fields, I will first explore the systematic effects of the choice of extinction and metallicity on the derived SFHs using the results for the H VIII field.

The effects of the value of the extinction on the derived SFH are shown in Figure 17 for the H VIII field in which the SFR and metallicity are plotted as a function of age assuming fixed values for the extinction of $A_V = 0.6, 0.9$ and 1.2 in the top, middle and bottom panels, respectively. As A_V increases, the best-fitting value of the current metallicity tends to decrease while leaving the initial metallicity unaffected. Holding the metallicity fixed and increasing the value of A_V (and the corresponding reddening) has the effect of making the main sequence redder while for a fixed value of the extinction, increasing the metallicity tends to make the main sequence bluer. Therefore, the SFH-fitting program attempts to compensate for the reddening of the main sequence for higher values of the extinction by decreasing the best-fitting current metallicity. In addition, increasing the extinction tends to increase the recent SFR as well as the ratio of young to old stars. However, there is a clear minimum in the value of the fit parameter for values of $A_V = 0.7 – 0.9$ for this field, as shown in Figure 18(a), where the fit parameter is plotted as a function of A_V .

In general the CMDs presented here do not go deep enough to place strong constraints on the age-metallicity relation in NGC 6822. The value of the fit parameter resulting from fitting the H VIII field CMD is shown in panels (b), (c) and (d) of Figure 18 as a function of the initial metallicity, final metallicity and chemical enrichment law, respectively. The value of the initial metallicity is not very well constrained by these CMDs. This is not entirely unexpected since all of the information about the SFH for ages > 1 Gyr is derived from the RGB and RC, areas of the CMD where the age and metallicity tend to be degenerate. There is a slight tendency for the fits to favor higher values of the final metallicity. The chemical enrichment laws 1 and 2 are somewhat favored over law 3 although the dependence of the fit parameter on the chemical enrichment law is slight.

The choice of age-metallicity relation does systematically affect the derived SFRs. The effects of the choice of initial metallicity and chemical enrichment law on the SFRs is illustrated in Figures 19 and 20. In each case, the final metallicity was held constant at a value of $[\text{Fe}/\text{H}]_f = -0.9$ while the initial metallicity was assumed to be $[\text{Fe}/\text{H}]_i = -2.3$ in Figure 19 and -1.4 for those solutions shown in Figure 20. In each figure, the SFR is shown on the left-hand side while the assumed age-metallicity relation is shown on the right. For low initial metallicities, the ratio of young to old stars tends to increase going from chemical enrichment laws 1 to 3, corresponding to a less rapid increase in metallicity with time. Furthermore, the SFR in the $7 – 15$ Gyr time bin decreases by a factor of $\sim 3 – 4$ as the initial metallicity goes from -2.3 to -1.4 . As would be expected, the three SFHs shown in Figure 20 for a higher initial metallicity are much more similar to one another. The

smaller difference in initial and final metallicities means that the choice of chemical enrichment law makes less of a difference in the resulting age-metallicity relation.

Keeping these systematic effects in mind, the approach adopted here is to average together the SFRs from some number of the solutions with the lowest value of the fit parameter. Unfortunately, as already discussed above, the only constraints presently available on the age-metallicity relation in NGC 6822 are the value of the current metallicity, as measured from the H II regions and individual massive stars, and the metallicity of the old cluster H VII. By averaging together the results from solutions resulting from different assumptions about the initial and final metallicities as well as the enrichment law, I may not necessarily obtain a more accurate result. However, the spread in SFRs resulting from these solutions allows an estimate to be made of the uncertainty in the SFR resulting from our ignorance of the chemical enrichment history in NGC 6822. Clearly, additional observations constraining the age-metallicity relation in this galaxy are needed to better understand its SFH.

As before, approximately 30 of the best solutions per field were used to calculate the average and standard deviation of the SFRs, metallicities and extinctions. The minimum and maximum fit parameters used as well as the best-fit value of the extinction for each field are shown in Table 6 while the corresponding SFRs for each field are listed in Table 7. The SFHs and corresponding metal enrichment histories for all the fields are plotted in Figures 21 and 22.

The most striking property of the SFHs in Figures 21 and 22 is the similarity in the SFH shapes for all five fields. The SFR appears to be constant or perhaps slightly increasing from 15 – 5 Gyr ago. Then after a decrease in the SFR from 3 to 5 Gyr ago, it rises back up to about the same level again in all the fields in the 0.6 – 3.0 Gyr age bin. The overall normalization of the SFR is somewhat higher in the H VI and H VII fields that lie in the bar than in the H IV, H VIII and C25 fields. The different average SFRs roughly correlate with the surface density of stars in each field. Thus, the bar contains a higher density of the old and intermediate age stars in addition to a higher density of younger stars.

The SFRs in the H VI and H VII fields, which have substantial overlap, agree to within the errors for stars older than 0.6 Gyr. The differences between the two fields are some indication of the internal consistency of the results presented here. For the two most recent time bins, the SFR in the H VI field is somewhat higher. The number of stars with $V - I < 0.7$ and $V < 23.5$ is 1902 in the H VI field and 1550 in the H VII field, a difference of about 20%. The higher recent SFR in the H VI field is thus the result of the higher density of bright blue stars compared to the H VII field.

It should be pointed out that the time bins chosen for this analysis are somewhat arbitrary. In particular, as is evident from Figure 7, the CMDs for stars with ages between about 1-7 Gyr are quite similar to one another. This means that the dip in the SFR in all fields 3-5 Gyr ago may not be very significant. Hence, the main conclusion to be drawn from the SFHs in Figures 21 and 22 is that overall the SFR in NGC 6822 has been fairly constant with no evidence for strong variations

with time.

These results derived using the full fits to the CMD from the Dolphin (1997) method are generally consistent with the old and intermediate age star formation history derived using the Gallart et al. (1996a) method. The best-fitting model is the one in which the star formation rate is either constant or shows a factor of four decrease in the last 5 Gyr compared to the older SFR. These two SFHs are plotted in Figure 23 along with the results for this field from Figure 22. While the SFHs derived from the two different methods are roughly consistent, the SFR from 5–15 Gyr ago is somewhat higher for SFH shape 4 than in the fit from the Dolphin (1997) method. This is likely a consequence of the requirement that the SFR is only allowed to decrease by a fixed factor of four.

4.3. Recent Star Formation Histories

The recent SFRs from the present to 0.6 Gyr ago show larger variations among the different fields. There is evidence for a recent increase in the SFR compared to the average past SFR in the H IV, H VI and H VII fields in which the star formation rate is about a factor of $\approx 3-4$ higher than the past star formation rate. On the other hand, the recent SFR in the H VIII and C25 fields is similar to or somewhat less than the past average rate. In fact the recent star formation in the C25 field is partly enhanced by OB association No. 15 from the identifications of Hodge (1977) which happens to fall partially on the WF4 chip in this field. Nevertheless, there are main sequence stars in this field that lie outside the OB association. These results confirm the conclusions of earlier ground-based observations that the sites of recent star formation in NGC 6822 are mostly confined to the bar while the older stars share a much wider distribution throughout the galaxy (e.g. Hodge 1977; Hodge et al. 1991). Furthermore, the differences in the ratio of current (0.6 Gyr ago to the present) SFRs to the older SFRs for the five fields are consistent with a picture in which stars that formed as long ago as 0.6 Gyr are not yet spatially very well mixed.

It is interesting to compare these results to the results derived from previous ground-based data. In particular, Gallart et al. (1996b) analyzed the SFH for the last 400 Myr and found evidence for an enhancement in the SFR throughout the galaxy in the last 100-200 Myr. The enhanced SFR was about a factor of two higher than the quiescent SFR in the central area of the bar as well as in the outer regions whereas the enhancement was found to be a factor of 4-6 in the regions at the northern and southern ends of the bar. I find an enhancement in the H IV field of a factor of 1.6 in the SFR about 200 Myr ago compared to the SFR for 200-600 Myr ago. For the H VI and H VIII fields I find a small enhancement in the most recent age bin while the SFRs determined here in the H VII and C25 fields are relatively constant from 600 Myr ago to the present. The most likely explanation for these differences between the *HST* and ground-based data is the small *HST* field-of-view. Apparently, the stars formed in the SFR enhancement detected by Gallart et al. (1996b) are still spatially clumped.

The recent star formation history for each field derived from the main sequence luminosity function (see §3.3) is plotted in Figure 24 as the solid red histogram while the dotted line shows the recent SFRs from Table 7. The H VI and H VII fields in the center of the bar show the highest SFR per area while the recent SFR in the C25 field is the lowest. Except for the outer C25 field, all of the recent SFHs show a small increase in the SFR starting about 200 Myr ago with a further increase detected in the H IV, H VI and H VII fields in the last 100 Myr. These trends are generally consistent with the the full SFH solutions. There is a tendency for the SFRs derived from the main sequence luminosity function to be smaller than the SFRs from the full fits to the CMD for ages > 200 Myr. This may be due in part to the selection of the region of the CMD used to construct the MS luminosity function. This limit was chosen to include as many MS stars as possible while minimizing the contamination by evolved stars. Due to the increase in photometric errors at fainter magnitudes (older ages) on the MS, some true MS stars may lie to the red of the adopted MS boundary, thus causing an underestimate of the SFR. The artificial star tests should account for this effect to some degree.

4.4. Extinction

The best-fitting values of the extinction in each field are listed in Table 6. These values are mainly determined by the color of the main sequence which is redder for those fields located within the bar compared to the fields sampling more of the outer regions. These values may be affected to some degree by the value of the final metallicity as discussed in §4.3. The extinction in the outer C25 field is $A_V = 0.72$, or $E(B - V) = 0.23$ while the extinction in the bar fields H IV, H VI and H VII reaches larger values of $A_V = 1.04 - 1.09$, or $E(B - V) = 0.34$, likely indicating some amount of extinction internal to NGC 6822. The extinction towards the C25 field is consistent with the Galactic foreground reddening of $E(B - V) = 0.22 - 0.26$ derived from the Galactic 100 μm dust emission (Schlegel et al. 1998). Similar results were also reached by Kayser (1967) who found $E(B - V) = 0.27 \pm 0.03$ based upon UBV photometry of foreground stars in the direction of NGC 6822. In contrast to these results, reddening based upon OB stars in NGC 6822 yield somewhat higher values of $E(B - V) = 0.42 \pm 0.05$ (van den Bergh & Humphreys 1979) and $E(B - V) = 0.45$ (Wilson 1992b). The observations of Massey et al. (1995) indicate an increase in the reddening from values of $E(B - V) = 0.26$ in the outer regions of NGC 6822 to values of $E(B - V) = 0.45$ near OB stars in the bar. The extinction values derived from the *HST* CMDs are consistent with these results although the A_V values measured here in the bar fields are not quite as high as the highest values found by Massey et al. (1995). The discrepancy may be due to the fact that the Massey et al. (1995) values are measured for a handful of massive individual stars while each of the extinctions in Table 6 represents an average over the entire WFPC2 field-of-view.

In Figure 25, the locations of the five WFPC2 fields are shown overlayed on the IRAS 60 μm map of NGC 6822 from Rice (1993). The corresponding value of A_V derived from the CMD fits is shown next to the location of each field. While there is a general correspondence between the

locations of FIR peaks and the luminous H II regions, these sources only account for about 50% of the total FIR emission in NGC 6822 with the remainder coming from a more diffuse component (Gallagher et al. 1991; Israel et al. 1996). As Gallagher et al. (1991) argued, the FIR is strong only in those locations where there is both a high UV radiation field and a significant amount of dust. Thus, one would expect there to be more FIR emission coming from those regions with both higher extinction and a high density of young, massive stars. A comparison of the extinction value for each field with the FIR flux at the same location is consistent with this expectation. The C25 field falls within an area with little FIR emission, consistent both with the low extinction measured for this field and the low current SFR there. The FIR flux is much higher within the H IV, H VI and H VII fields where the CMDs indicate higher extinctions and higher recent SFRs. Although the extinction and recent SFR derived from the H VIII field is only slightly larger than for the C25 field, there is substantial FIR flux in this area. However, the FIR peak within the H VIII field is coincident with H X, perhaps indicating that most of the FIR emission in this area is coming from this H II region. In fact, O’Dell et al. (1999) found that the CMD of the stars in H X is consistent with a reddening of $E(B - V) = 0.35$ ($A_V = 1.1$), a value somewhat higher than the value of $A_V = 0.82$ derived here for the field near H X. This difference would be consistent with most of the dust in this field being mostly in the vicinity of the H II region H X.

4.5. Comparison of Model and Observed Color-Magnitude Diagrams

Using the model SFHs plotted in Figures 21 and 22, model CMDs for each field were constructed and are plotted together in Figure 26 which can be directly compared to the observed CMDs in Figure 2. Another method of displaying a CMD is the Hess diagram, which is a surface that indicates the number of stars within a series of color and magnitude bins in the CMD. Hess diagrams of each of the observed and model diagrams were constructed for each field using the same CMD bins used in the SFH solution. In each panel of Figure 27, the difference between the model and observed Hess diagrams divided by the model diagram is shown. Each diagram is displayed from a ratio of -1.5 (black) to 1.5 (white).

Overall, the model CMDs reproduce the general morphology of the observed data. There are important differences, however. Generally, the main sequence in all of the fields is somewhat broader than predicted simply based upon the results of the artificial star tests. This may be due to my assumption of a single extinction in each field when in reality there may be significant variation in the extinction along the line-of-sight through NGC 6822. This interpretation is supported by the tendency for there to be more observed stars than predicted redward of the model main sequence. Another possibility is that binaries may cause the main sequence to be somewhat broader than predicted. A second difference apparent between the models and observations is the distribution of stars in the red clump. The observed red clump is tilted upward in the diagram. This results in an underabundance of model stars brightward and blueward of the model clump while the models have too many stars on the red and faint end of the clump. A similar discrepancy is apparent

in the SFH fits for the dwarf galaxy WLM (Dolphin 1999). One possible explanation could be differential reddening within the field since the shape of the red clump is roughly parallel to the reddening vector. In addition to these differences, the asymptotic giant branch (AGB) population is evident in the models CMDs extending brighter and redder of the RGB and is absent in the observed CMDs. However, the saturation limit of $I \approx 19$ renders much of the AGB unmeasured in the observations.

A fourth difference between the models and observations is apparent in the area of the “blue loops” between the RGB and the main sequence. These are evolved intermediate to massive stars undergoing core He fusion. As is apparent from all the model CMDs, these stars tend to lie along two sequences, one to the red and the other to the blue. The magnitude of stars on both sequences increases with decreasing mass with both sequences eventually merging into the RC. The stars initially start on the red sequence and then loop over to the blue sequence where they spend most of the remainder of their He-burning lifetime. The amount of time stars spend on the blue loops as well as the details of the evolution depend upon a number of somewhat uncertain physical details, such as the nuclear reaction rates and the extent of the convective core, among other details (Chiosi et al. 1992). In addition, the color of the blue end of the loops increases with metallicity with the loops disappearing near solar metallicity (Bertelli et al. 1994). In the H VI and H VII fields there is a hint of a sequence of red supergiants marking the red end of the blue loops while the blue end of the loops, if present, is even weaker. The relative lack of identifiable sequences in the observed CMDs may be due to some combination of effects including differential extinction, binaries and uncertainties in the input physics to the evolutionary models. In addition, there are likely a number of foreground Galactic stars contaminating this portion of the diagram. A similar situation is apparent in the ground-based CMDs analyzed by Gallart et al. (1996a). In their CMD, the red end of the loops is clearly visible while the blue end of the loops appears to merge with the main sequence. Gallart et al. (1996a) interpreted this as evidence for differential extinction within their data.

4.6. Discussion

It is important to point out that the ages and SFHs derived in the previous sections are based, among other things, on the assumption that the distance to NGC 6822 is 500 kpc. This distance was determined from observations of the Cepheids and assuming a distance modulus to the LMC of $(m - M)_0 = 18.5$. However, the distance modulus to the LMC remains controversial. Van den Bergh (2000) found that an average of 18 of the most recent distance measurements yields a value of $(m - M)_0 = 18.49$ while the individual determinations range all the way from 18.1 to 18.7. In addition, the implications of the *HIPPARCOS* mission on the distance scale remain controversial. (See discussions in van den Bergh 2000 and Walker 1999).

Changing the assumed distance to NGC 6822 would have an effect on the intermediate and old SFH because shifting the inferred limits of the RGB bins shown in Figure 10 would change

the color of the red edge of the RGB. Using the methods presented in §3.2, this might lead to a younger or older age for the oldest stars. However, as can be seen in Figure 14, the shape of the RGB is also affected by the age of the oldest stars. The RGB width and shape are of course not affected by changes in the distance. Based upon tests of his SFH-fitting method on artificial data for a model galaxy, Dolphin (1997) found that errors in the distance modulus tended to affect the SFRs determined for the older stars while leaving the recent SFRs relatively unaffected. For an error in the distance modulus of ± 0.06 mag, Dolphin (1997) determined that the SFRs in the 5-10 and 10-15 Gyr age bins could systematically change by as much as 40%. The SFR averaged over the entire 5-15 Gyr age range though was only off by at most 10%. Therefore, the results presented here for the age of the oldest stars and the SFHs would probably not be affected to a large degree if the distance to the LMC were revised somewhat.

From the SFHs presented in §4.2, it is apparent that the SFH shapes among the five fields are similar for older ages but diverge within the last 0.5 Gyr, implying that stars formed with ages up to 0.5 Gyr are not well mixed throughout the galaxy. This mixing time scale of ~ 0.5 Gyr derived from the SFH solutions can be compared with other dynamical time-scales in NGC 6822. The velocity dispersion of the H I gas in NGC 6822 varies between about 7-10 km/s across its major axis (de Blok & Walter 2000). Assuming that stars are formed with a similar velocity dispersion, the implied time scale is given by

$$\frac{D}{\sigma_{HI}} = \frac{2.9 \text{ kpc}}{7 \text{ km/s}} = 0.4 \text{ Gyr} \quad (7)$$

where D is the optical diameter of the galaxy. A second relevant time scale is the rotation period as measured from the H I gas. At a radius of 1.4 kpc, the rotation speed is about 35 km/s (Gottesman & Weliachew 1977; de Blok & Walter 2000) which corresponds to a rotation period of 0.3 Gyr. Both of these time scales are similar to the mixing times implied by the differences in the recent SFRs among the five HST fields analyzed here.

The enhancement in the SFR 100-200 Myr ago detected in the ground-based data of Gallart et al. (1996b) was also detected in perhaps two out of the five HST pointings analyzed in this paper. In addition to the evidence from ground-based and *HST* CMDs, a period of increased activity in NGC 6822 around this time is also supported by the increase in the cluster formation rate 75-100 Myr ago detected by Hodge (1980). The low N/O ratio in NGC 6822 is consistent with a recent episode of increased star formation as well (Skillman et al. 1989b). Oxygen is a primary nucleosynthesis product produced in massive stars while nitrogen may be produced primarily as a secondary nucleosynthesis product via the CNO cycle in intermediate mass stars (e.g., see discussion in Smith 1975). As pointed out by Skillman et al. (1989b), for example, the low N/O ratio in NGC 6822 points to a scenario in which a recent increase in the SFR enriched the ISM with oxygen. If the increase happened recently enough, there may not have been enough time for intermediate mass stars to leave the main sequence and elevate the nitrogen abundance.

As NGC 6822 occupies a relatively isolated position in the Local Group (e.g. Mateo 1998), interactions with other known galaxies are not the likely cause of this recent SFR enhancement.

De Blok & Walter (2000) discussed the possibility that interaction between the main body of NGC 6822 and the H I cloud in the extreme NW of the galaxy may be responsible for the increased star formation. According to their data, the NW H I complex has a total H I mass of $\sim 1.4 \times 10^7 M_\odot$. In addition, the H I velocity undergoes a sharp jump at the boundary between the cloud and the rest of NGC 6822, perhaps indicating that it is actually a separate system. Furthermore, one-half the rotation period of the cloud is ~ 300 Myr, a time scale comparable to the time-scale derived from the recent SFH.

The recent SFHs derived from the *HST* CMDs can also be compared with estimates of the current SFR from both the H α and far infra-red (FIR) emission of NGC 6822. The total H α luminosity due to the catalogued H II regions in NGC 6822 is 3.0×10^{39} ergs s $^{-1}$ (Hodge et al. 1989) for a distance of 500 kpc and reddening of $E(B-V) = 0.24$. This implies a current SFR of $\geq 3 \times 10^{-9} M_\odot \text{ yr}^{-1} \text{ pc}^{-2}$ where I have adopted the SFR(H α) calibration of Kennicutt (1998a) and assumed a circular area for NGC 6822 with radius 1.4 kpc. The SFR derived from the H α luminosity is a lower limit because it excludes any possible diffuse H α emission that may be ionized by Lyman continuum photons that escape H II regions and whose contribution should be included when calculating the current SFR. On the other hand, the FIR luminosity of NGC 6822 at wavelengths of 60 – 100 μm is $5 \times 10^7 L_\odot$ (Gallagher et al. 1991). Under the assumption that the FIR emission in galaxies is due to dust heated by stars with masses $M \geq 2M_\odot$ and that the stellar luminosity is converted into L_{FIR} with some efficiency η , the SFR averaged over the past Gyr can be calculated from L_{FIR} (Hunter et al. 1989). Gallagher et al. (1991) argued that $\eta \leq 0.5$, implying that the recent SFR in NGC 6822 is $\geq 0.04 M_\odot \text{ yr}^{-1}$, or $\geq 7 \times 10^{-9} M_\odot \text{ yr}^{-1} \text{ pc}^{-2}$, averaged over the same area as for the H α SFR. Both the H α and L_{FIR} SFR calibrations assume a Salpeter IMF extending from 0.1 to 100 M_\odot . These lower limits for the average recent SFRs derived from the H α and FIR emission are comparable to the SFR per area in the C25 and H VIII fields while the other three *HST* fields have somewhat higher SFRs per area over the past 200 Myr.

There are a few other isolated dwarf irregular galaxies in the Local Group besides NGC 6822 whose star formation histories have been studied in similar detail. All of the evidence suggests that IC 1613 ($M_B = -14.6$) has had an evolutionary history not radically different from that of NGC 6822. RR Lyrae stars have been detected in IC 1613, indicating that star formation began in this galaxy at least 10 Gyr ago (Saha et al. 1992). Based upon *VI* CMDs from *HST*, Cole et al. (1999) detected the presence of a horizontal branch indicative of an old stellar population. Cole et al. (1999) also detected a number of asymptotic giant branch stars and a strong RC implying that there is a strong intermediate age (1-10 Gyr old) population in IC 1613 as well. While the dwarf galaxy WLM ($M_B = -13.8$) has a single globular cluster with an age of about 15 Gyr, it most likely began forming significant numbers of field stars ~ 12 Gyr ago with about 50% of its stars formed 9-12 Gyr ago (Hodge et al. 1999; Dolphin 2000a). Although the errors are large, star formation may have decreased 2.5-9 Gyr ago before increasing again in the central regions within the past Gyr (Dolphin 2000a). Based upon an analysis similar to that used by Gallart et al. (1996a) to study NGC 6822, Aparicio et al. (1997) found that their ground-based CMDs of the dwarf galaxy

Pegasus were best fit with star formation beginning about 15 Gyr ago and then remaining constant or perhaps gradually declining from then to the present. Using CMDs from *HST*, Gallagher et al. (1998) argued that the star formation rate in this galaxy was about a factor of 3-4 higher about a Gyr ago than at present. Despite the differences in the their total luminosities, these three isolated dwarf irregulars are all similar to NGC 6822 in that they seem to have formed stars at more or less a constant rate throughout their lifetimes with no evidence for very strong variations greater than a factor of $\approx 3 - 4$. All three galaxies are also similar to NGC 6822 in that they most likely began forming stars about 12-15 Gyr ago. The one Local Group dwarf irregular galaxy whose star formation history is an exception to the others is Leo A. Based upon the distribution of stars in the RC and blue loops in the CMD, Tolstoy et al. (1998) argued that a major episode of star formation occurred in Leo A 0.9-1.5 Gyr ago. Furthermore, these authors concluded that at least 90% of the stars in Leo A formed in the past 2 Gyr.

The SFHs for NGC 6822 derived here along with a stellar population synthesis code can be used to infer the integrated absolute magnitude of NGC 6822 as a function of time. Assuming a Salpeter IMF between 0.1 and $120 M_{\odot}$, no internal extinction and that the SFH derived from the H VIII field is representative, I have used the galaxy evolution code PEGASE (Fioc & Rocca-Volmerange 1997) to determine the absolute B and V magnitudes of NGC 6822 as a function of look-back time. For an assumed SFH, metal enrichment history, IMF and internal extinction, the PEGASE code calculates the integrated spectrum for both the stars and gas as a function of time, assuming a total mass of stars formed of $1 M_{\odot}$. This spectrum is then convolved with a list of filter transmission curves to determine the magnitudes and colors of the model galaxy in each of the filters. I have scaled the normalized magnitudes for the H VIII field SFH by requiring that the present V absolute magnitude of the model galaxy match the observed value of $M_V = -16.1$.

The results are plotted in Figure 28 in which the rest-frame B and V absolute magnitudes for NGC 6822 are plotted as a function of look-back time from the present. The overall trend is a gradual increase in the luminosity of the galaxy with time. The increase in absolute magnitude about 4 Gyr ago corresponds to the drop in the SFR around this time. As discussed in §4.2 and illustrated in Figure 7, this drop in the SFR may not be very significant given the similarity of the CMDs for stars between 1 and 7 Gyr old. For comparison the corresponding redshift is plotted on the upper axis assuming a flat, cosmological constant dominated cosmology with a Hubble constant of $H_0 = 75 \text{ km s}^{-1} \text{ Mpc}^{-1}$ and $\Omega_{\Lambda} = 0.7$. In the I -band selected CFRS redshift survey (Lilly et al. 1995), the faintest galaxies have $M_{AB}(B) = -16$, compared to the current absolute magnitude of NGC 6822 of $M_{AB}(B) = -15.6$. Galaxies with similar masses and evolutionary histories to NGC 6822 are therefore not likely to be contributing to the evolving population detected in the CFRS survey. In the b_j selected Autofib redshift survey (Ellis et al. 1996), the galaxies span the apparent magnitude range $11.5 < b_j < 24.0$ and have redshifts in the range $0 < z < 0.75$. Galaxies like NGC 6822 would be detectable in the Autofib data out to redshifts of $z \approx 0.2$. Assuming the b_j K-corrections of King & Ellis (1985) for an Sdm galaxy and the same cosmology as in Figure 28 ($H_0 = 75 \text{ km s}^{-1} \text{ Mpc}^{-1}$, $\Omega = 1$, $\Omega_{\Lambda} = 0.7$), NGC 6822 would fade to $b_j \approx 27.4$ mag at $z = 0.75$.

Hence, galaxies similar to NGC 6822 are not likely contributing to the faint blue galaxy excess in either the Autofib or CFRS redshift surveys.

The one caveat to this conclusion is that the age resolution of the SFH solutions presented here decreases dramatically with age. If most of the star formation at older ages occurred in one or more short bursts, it may be possible that a galaxy such as NGC 6822 would become momentarily bright enough to be detected in these redshift surveys before fading again. As an example, I have recalculated the evolution of the integrated absolute magnitude of NGC 6822 as a function of age with the PEGASE code assuming that all of the stars formed in the 5 – 7 Gyr time bin were formed in a single star formation burst of varying duration centered at an age of 6 Gyr. The results are that NGC 6822 would temporarily brighten during the burst to an absolute magnitude of $M_B = -19.5$, -17.7 and -16.7 for star formation bursts of duration 10, 100 and 500 Myr, respectively. In the redshift range $0.50 < z < 0.75$, the CFRS detected galaxies down to $M_{AB}(B) \simeq -19.5$. Since an age of 6 Gyr corresponds to $z \approx 0.6$, a galaxy similar to NGC 6822 would only be detectable if all of the star formation in the 5 – 7 Gyr time bin were squeezed into a 10 Myr long star formation burst. At $z = 0.6$, the corresponding apparent b_j magnitudes would be 22.8, 24.6 and 25.6 for the 10, 100 and 500 Myr bursts, respectively. Since the Autofib survey included galaxies down to $b_j = 24$, only a galaxy undergoing a star burst of duration 10 Myr would be bright enough to make it into that survey as well.

If there were such an intense burst of star formation in NGC 6822 5 – 7 Gyr ago, it would be difficult to detect with the CMDs presented in this paper due to the relatively poor age resolution of the RC and RGB structures in these diagrams where stars with these ages would be found. The main sequence turn-off for 6 Gyr old stars occurs at $M_V \approx 3.5$ (Bertelli et al. 1994), which at the distance and extinction of NGC 6822 corresponds to an apparent magnitude of $V \approx 27.7$, a level clearly much fainter than the current data. Without deeper photometry reaching much farther down the main sequence, it is not possible to determine if such a star formation burst occurred in NGC 6822 or not. The recent enhancement by a factor of 2-4 in the SFR 100-200 Myr ago detected by Gallart et al. (1996b) argues that the SFR in NGC 6822 likely has varied by similar amounts throughout its history. Nevertheless, even if this is the case, variations of that size would not be enough to render galaxies like NGC 6822 detectable in the current generation of redshift surveys.

5. Summary

This paper presents the first study of the star formation history of the dwarf irregular galaxy NGC 6822 based upon *HST* CMDs of five fields. The main conclusions of this study are summarized below.

- 1) The best-fitting value of the extinction in the outer-most C25 field is $A_V = 0.72$, a value consistent with the expected amount of Galactic foreground extinction toward NGC 6822. In the H IV, H VI and H VII fields in the bar, the extinction is $\approx 0.3 – 0.4$ magnitudes higher, presumably

due to absorbing dust internal to NGC 6822.

2) The distribution of stars along the RGB implies that star formation in NGC 6822 began 15 Gyr ago. This conclusion rests upon two critical assumptions: 1) that stars began forming from low-metallicity gas, as indicated by the age and metallicity of the cluster H VII, and 2) that there is no spread in metallicity at a given age. If the initial metallicity were higher or if the metal enrichment were rapid, then the CMD could be fit by star formation beginning at younger ages. Metallicities derived from spectra of individual RGB stars would be useful in constraining the early chemical enrichment history of NGC 6822.

3) Using the methods developed by Dolphin (1997), the SFH in each field was extracted. The overall shape of the SFH is quite similar among the five fields with a higher overall SFR per area in the bar fields compared to the C25 and H VIII fields covering more out-lying regions. In all five fields, except for a possible dip in the SFR from 3 to 5 Gyr ago, the SFR has been fairly constant or perhaps somewhat increasing from 15 Gyr ago to the present. For the H VIII field, the color distribution of stars along the RGB was used to constrain the SFH via the method developed by Gallart et al. (1996a). The results are similar to the conclusions drawn from the Dolphin (1997) method. A SFH in which star formation begins 12-15 Gyr ago and is either constant or undergoes a factor of four decrease about 5 Gyr ago is best able to fit the observed RGB.

4) While the old and intermediate age SFHs of all five fields are similar, the ratio of the recent SFR (< 0.6 Gyr old) to the average past rate varies among the five fields. The H IV, H VI and H VII fields in the bar show an increase by about a factor of 3-4 in the SFR in the past 0.6 Gyr compared to the average past rate. The remaining two fields that cover more of the outer regions of the galaxy show a SFR that is roughly the same or somewhat less than the average past rate. These results imply that stars less than about 600 Myr old are not spatially well-mixed throughout the galaxy. This is consistent with a scenario in which stars form in OB associations and then slowly diffuse throughout the galaxy. The time-scale derived from the analysis of the CMDs is similar to the dynamical time-scales estimated from the rotation and velocity dispersion of the H I gas.

5) Model CMDs constructed from the best-fitting SFHs match the overall morphology of the observed diagrams although there are differences mainly in the area of the red clump and blue loops where the stellar evolutionary models are more uncertain. The observed main sequence is also somewhat broader in the observations compared to the models, particularly in the bar fields. This may be due to the presence of binary stars or differential extinction within each field which are both not included in the models.

6) The SFH for the H VIII field was used as input to the PEGASE (Fioc & Rocca-Volmerange 1997) galaxy evolution code to infer the absolute *BV* integrated magnitude of NGC 6822 as a function of look-back time and redshift. In the rest-frame *B* and *V* bands NGC 6822 gradually brightens with decreasing redshift except for a temporary decrease in the luminosity during the lull in star formation 3-5 Gyr ago. For a flat cosmology with $H_0 = 75 \text{ km s}^{-1} \text{ Mpc}^{-1}$ and $\Omega_\Lambda = 0.7$, galaxies with evolutionary histories similar to NGC 6822 would be undetectable in the CFRS

redshift survey (Lilly et al. 1995) and would be included in the Autofib survey (Ellis et al. 1996) only out to a redshift of $z \approx 0.2$. However, if most of the stars older than a Gyr were formed in a single short burst of star formation, such a galaxy might then have been bright enough to become detectable in the current generation of redshift surveys. In particular, if all of the star formation from 5 to 7 Gyr ago were compressed into a burst lasting only 10 Myr, a galaxy similar to NGC 6822 would temporarily rise above the detection limits of both the CFRS and Autofib surveys.

I am grateful to Andrew Dolphin for providing me with his HSTPHOT/MULTIPHOT photometry package as well as many of the computer programs used in deriving the star formation histories presented in this paper. I also wish to thank Julianne Dalcanton and Eugene Magnier for helpful comments. I am particularly grateful to my thesis advisor Paul Hodge for all his excellent help and guidance throughout this project. I also wish to thank the anonymous referee for carefully reading the manuscript and for making many insightful comments which have significantly improved this paper. Partial support for this work was provided by NASA through grant numbers GO-08314 and AR-08362 from the Space Telescope Science Institute, which is operated by the Association of Universities for Research in Astronomy, Incorporated, under NASA contract NAS5-26555.

REFERENCES

Aparicio, A., Gallart, C., & Bertelli, G. 1997, AJ, 114, 669

Armandroff, T.E. & Massey, P. 1985, ApJ, 291, 685

Babul, A. & Ferguson, H.C. 1996, ApJ, 458, 100

Babul, A. & Rees, M.J. 1992, MNRAS, 255, 346

Bertelli, G., Bressan, A., Chiosi, C., Fagotto, F., & Nasi, E. 1994, A&AS, 106, 275

Bertelli, G. & Nasi, E. 2001, AJ, 121, 1013

Chandar, R., Bianchi, L., & Ford, H.C. 2000, AJ, 120, 3088

Chiosi, C., Bertelli, G., & Bressan, A. 1992, ARA&A, 30, 235

Cohen, J.G. & Blakeslee, J.P. 1998, AJ, 115, 2356

Cole, A.A. et al. 1999, AJ, 118, 1657

Collier, J., Hodge, P., & Kennicutt, R.C. 1995, PASP, 107, 361

Cook, K.H., Aaronson, M., & Norris, J. 1986, ApJ, 305, 634

Davies, R.D. 1972, in IAU Symposium No. 44, External Galaxies and Quasi-stellar Objects, edited by David S. Evans (Reidel, Dordrecht), p. 67

de Blok, W.J.G. & Walter, F. 2000, ApJ, 537, L95

Dohm-Palmer, R.C., Skillman, E.D., Saha, A., Tolstoy, E., Mateo, M., Gallagher, J., Hoessel, J., Chiosi, C., & Dufour, R.J. 1997, AJ, 114, 2527

Dolphin, A. 1997, New Astronomy, 2, 397

Dolphin, A. 1999, Ph.D. Thesis, University of Washington

Dolphin, A.E. 2000a, ApJ, 531, 804

Dolphin, A.E. 2000b, PASP, 112, 1383

Dolphin, A.E. 2000c, PASP, 112, 1397

Ellis, R.S. 1997, ARA&A, 35, 389

Ellis, R.S., Colless, M., Broadhurst, T.J., Heyl, J.S., & Glazebrook, K. 1996, MNRAS, 280, 235

Fioc, M. & Rocca-Volmerange, B. 1997, A&A, 326, 950

Gallagher, J.S., Hunter, D.A., Gillet, F.C., & Rice, W.L. 1991, *ApJ*, 371, 142

Gallagher, J.S., Tolstoy, E., Dohm-Palmer, R.C., Skillman, E.D., Cole, A.A., Hoessel, J.G., Saha, A., & Mateo, M. 1998, *AJ*, 115, 1869

Gallart, C., Aparicio, A., Bertelli, G., & Chiosi, C. 1996a, *AJ*, 112, 1950

Gallart, C., Aparicio, A., Bertelli, G., & Chiosi, C. 1996b, *AJ*, 112, 2596

Gallart, C., Aparicio, A., & Víchez, J.M. 1996c, *AJ*, 112, 1928

Girardi, L., Bressan, A., Chiosi, C., Bertelli, G., & Nasi, E. 1996, *A&AS*, 117, 113

Girardi, L., Bressan, A., Bertelli, G., & Chiosi, C. 2000, *A&AS*, 141, 371

Gottesman, S.T. & Weliachew, L. 1977, *A&A*, 61, 523

Grillmair, C.J. et al. 1998, *AJ*, 115, 144

Hernandez, X., Valls-Gabaud, D., & Gilmore, G. 1999, *MNRAS*, 304, 705

Hodge, P.W. 1977, *ApJS*, 33, 69

Hodge, P.W. 1980, *ApJ*, 241, 125

Hodge, P.W. 1989, *ARA&A*, 27, 149

Hodge, P., Kennicutt, R.C., & Lee, M.G. 1988, *PASP*, 100, 917

Hodge, P., Lee, M.G., & Kennicutt, R.C. 1989, *PASP*, 101, 32

Hodge, P., Smith, T., Eskridge, P., MacGillivray, H., & Beard, S. 1991, *ApJ*, 379, 621

Hodge, P.W., Dolphin, A.E., Smith, T.R., & Mateo, M. 1999, *ApJ*, 521, 577

Hoessel, J.G. & Anderson, N. 1986, *ApJS*, 60, 507

Holtzman, J.A. et al. 1995a, *PASP*, 107, 156

Holtzman, J.A., Burrows, C.J., Stefano, C., Hester, J.J., Trauger, J.T., Watson, A.M., & Worthey, G. 1995b, *PASP*, 107, 1065

Holtzman, J.A. et al. 1999, *AJ*, 118, 2262

Hubble, E. 1925, *ApJ*, 62, 409

Hunter, D.A., Gallagher, J.S., Rice, W.L., & Gillett, F.C. 1989, *ApJ*, 336, 152

Hurley-Keller, D., Mateo, M., Nemec, J. 1998, *AJ*, 115, 1840

Hutchings, J.B., Cavanagh, B., & Bianchi, L. 1999, PASP, 111, 559

Israel, F.P. 1997, A&A, 317, 65

Israel, F.P., Bontekoe, Tj.R., & Kester, D.J.M. 1996, A&A, 308, 723

Kayser, S.E. 1967, AJ, 72, 134

Kennicutt, R.C. 1998a, ARA&A, 36, 189

Kennicutt, R.C. 1998b, in The Stellar Initial Mass Function, edited by G. Gilmore and D. Howell (Astronomical Society of the Pacific Conference Series, San Francisco), p. 1

King, C.R. & Ellis, R.S. 1985, ApJ, 288, 456

Kurucz, R.L. 1992, in Stellar Populations of Galaxies, eds. B. Barbuy and A. Renzini (Kluwer, Dordrecht), p. 225

Lee, M.G., Freedman, W.L., & Madore, B.F. 1993, ApJ, 417, 553

Lequeux, J., Peimbert, M., Rayo, J.F., Serrano, A., & Torre-Peimbert, S. 1979, A&A, 80, 155

Lilly, S. J., Tresse, L., Hammer, F., Crampton, D., & Le Fèvre, O. 1995, ApJ, 455, 108

Marconi, G., Tosi, M., Greggio, L., & Focardi, P. 1995, AJ, 109, 173

Massey, P., Armandroff, T.E., Pyke, R., Patel, K., & Wilson, C.D. 1995, AJ, 110, 2715

Mateo, M. 1998, ARA&A, 36, 435

McAlary, C.W., Madore, B.F., McGonegal, R., McLaren, R.A., & Welch, D.L. 1983, ApJ, 273, 539

Mighell, K.J & Burke, C.J. 1999, AJ, 118, 366

Muschielok, B., et al. 1999, A&A, 352, L40

O'Dell, C.R., Hodge, P.W., & Kennicutt, R.C. 1999, PASP, 111, 1382

O'Donnell, J.E. 1994, ApJ, 422, 158

Olsen, K.A.G. 1999, AJ, 117, 2244

Pagel, B.E.J., Edmunds, M.G., & Smith, G. 1980, MNRAS, 193, 219

Peimbert, M. & Spinrad, H. 1970, A&A, 7, 311

Roberts, M. 1972, in IAU Symposium No. 44, External Galaxies and Quasi-stellar Objects, edited by David S. Evans (Reidel, Dordrecht), p. 12

Rice, W. 1993, AJ, 105, 67

Saha, A., Freedman, W.L., Hoessel, J.G., & Mossman, A.E. 1992, AJ, 104, 1072

Salpeter, E.E. 1955, ApJ, 121, 161

Schechter, P.L., Mateo, M., & Saha, A. 1993, PASP, 105, 1342

Schlegel, D.J., Finkbeiner, D.P., & Davis, M. 1998, ApJ, 500, 525

Skillman, E.D., Kennicutt, R.C., & Hodge, P.W. 1989a, ApJ, 347, 875

Skillman, E.D., Terlevich, R., & Melnick, J. 1989b, MNRAS, 240, 563

Smecker-Hane, T.A., Stetson, P.B., Hesser, J.E., & Lehnert, M.D. 1994, AJ, 108, 507

Smith, H.E. 1975, ApJ, 199, 591

Stetson, P.B. 1994, PASP, 106, 250

Tolstoy, E. & Saha, A. 1996, ApJ, 462, 672

Tolstoy, E., Galagher, J.S., Cole, A.A., Hoessel, J.G., Saha, A., Dohm-Palmer, R.C., Skillman, E.D., Mateo, M., & Hurley-Keller, D. 1998, AJ, 116, 1244

van den Bergh, S. 2000, The Galaxies of the Local Group, (Cambridge, Cambridge University Press)

van den Bergh, S. & Humphreys, R. M. 1979, AJ, 84, 604

Venn, K.A., et al. 2001, ApJ, 547, 765

Walker, A.R. 1999, in Post-Hipparcos Cosmic Candles, edited by A. Heck and F. Caputo (Kluwer, Dordrecht), p. 125

Wheeler, J.C., Sneden, C., & Truran, J.W. 1989, ARA&A, 27, 279

Whitmore, B., Heyer, I., & Casertano, S. 1999, PASP, 111, 1559

Wilson, C.D. 1992a, ApJ, 391, 144

Wilson, C.D. 1992b, AJ, 104, 1374

Wilson, C.D. 1994, ApJ, 434, L11

Wyder, T.K., Hodge, P.W., & Zucker, D.B. 2000, PASP, 112, 1162

Fig. 1.— Digitized Sky Survey image of NGC 6822. The entire field-of-view is $15' \times 15'$ with North up and East to the left. The positions of the five WFPC2 fields analyzed here are shown. Each field is labeled by the cluster or H II region that is centered on the PC chip. The cluster C25 is from the list of clusters in Hodge (1977) while the remaining objects labeled with an H were originally identified by Hubble (1925).

Fig. 2.— Observed V , $V - I$ CMDs for all stars detected in the WF chips of each field. The contour levels correspond to stellar densities of 20, 40, 60, 80, 100, 150, 200, 300, 400, and 500 stars decimag^{-2} . For those areas of each CMD with fewer than 20 stars decimag^{-2} , each individual star is plotted. See Figure 1 for the positions of these fields in NGC 6822.

Fig. 3.— Fraction of the artificial stars recovered in both V and I as a function of the input V magnitude for all five fields. Each panel is labeled with the corresponding field name. The solid, dotted and dashed lines are the completeness curves for artificial stars with input $(V - I)$ colors of -0.5 to 0.5 , 0.5 to 1.5 , and 1.5 to 2.5 , respectively.

Fig. 4.— The fraction of stars from the H VII photometry that were also detected in the H VI field as a function of V magnitude (solid line). Only stars in the H VII field that lie within the field-of-view of the H VI field were included in the calculation. The dotted line shows the probability that a star should be detected on both fields based upon the results of the artificial star tests. This prediction is simply the product of the completeness fractions for the H VI and H VII fields for artificial stars with input colors $0.5 < V - I < 1.5$. The agreement between the observed and predicted fractions argues that the artificial star tests provide an accurate description of the completeness.

Fig. 5.— (a) The expected error in the V photometry σ_V derived from the artificial star tests for the H VI field (pluses) and H VII field (diamonds). (b) The difference in V magnitude ΔV divided by the expected error as a function of magnitude for stars detected in both the H VI and H VII fields. The differences are in the sense of the H VI minus the H VII photometry. Panels (c) and (d) are the same as (a) and (b) except the I -band results are plotted.

Fig. 6.— The three chemical enrichment laws used as the input for each SFH solution using the Dolphin (1997) method for an initial metallicity of $[\text{Fe}/\text{H}] = -2.3$ and a final metallicity of $[\text{Fe}/\text{H}] = -0.7$. The solid, dotted and dashed curves in this figure are referred to in the text as chemical enrichment laws (CELs) 1, 2 and 3, respectively.

Fig. 7.— Model CMDs, separated by age, generated from the H VIII field artificial star test results. These CMDs assume a constant SFR of $5 \times 10^{-4} M_\odot \text{ yr}^{-1}$, an initial metallicity of $[\text{Fe}/\text{H}] = -2.3$ and a final metallicity of $[\text{Fe}/\text{H}] = -0.7$ and chemical enrichment law 2, as plotted in Figure 6.

Fig. 8.— Three different SFH solutions for the H VIII field assuming three different sets of time bins. In panel (a), the results for Test 1 are shown for all 12 time bins used in the solution. In panel (b), the same solution is shown, rebinned to match the time bins used in the results

presented in §4 of the text. The results for Test 2 (32 time bins with spacing $\Delta \log(t) = 0.1$) are shown panels (c) and (d) while panels (e) and (f) show the results for Test 3 (16 time bins with spacing $\Delta \log(t) = 0.2$).

Fig. 9.— The five possible input star formation history shapes tried. The youngest age considered has been set to $T_f = 10$ Myr while T_i is the age of the oldest stars. For all shapes, except the constant SFR case (Shape 3), the higher SFR is four times the lower SFR. Each of the time bins is 1/3 of T_i in length and all three curves have been normalized to have the same integrated mass of stars formed. These shapes are identical to those assumed by Gallart et al. (1996a).

Fig. 10.— The H VIII CMD assuming a distance modulus of 23.49 and extinction of $A_V = 0.82$. The regions marked with the numbers 1 to 4 indicate the regions of the red giant branch used to compare the models and observations while the region labeled RC is defined to be the red clump region. All stars that lie blueward of the dashed line are assumed to be main sequence stars when computing the main sequence luminosity function.

Fig. 11.— Model RGB color distributions (solid lines) assuming $Z_i = 0.0001$ ($[\text{Fe}/\text{H}] = -2.3$) for the stars within the RGB region 1 shown in Figure 10. The number in the upper left-hand corner of each panel indicates the SFH shape used in the model. Each of the columns shows the model RGB color distributions for four values of T_i (from left to right): 15, 12, 9 and 6 Gyr. In each panel the observed color distribution is plotted as the dotted line.

Fig. 12.— The fit parameter $\bar{\chi}^2$ as a function of the time when star formation begins (T_i) for different assumptions regarding the metal enrichment history. Each panel shows the variation of the fit parameter with T_i for a particular choice of initial metallicity $[\text{Fe}/\text{H}]_i$ and the final metallicity $[\text{Fe}/\text{H}]_f$ for the three different metal enrichment laws shown in Figure 6. The solid, dotted and dashed lines correspond to the chemical enrichment laws 1, 2 and 3, respectively. An extinction of $A_V = 0.8$ mag was assumed for all of the solutions plotted here.

Fig. 13.— Best-fit star formation and chemical enrichment histories for the H VIII field under three different assumptions of the age of the oldest stars T_i . The results are shown for $T_i = 15, 12$ and 9 Gyr in the top, middle and bottom panels, respectively.

Fig. 14.— Model CMDs for the H VIII field under three different assumption for the age of the oldest stars T_i : (a) 15 Gyr, (b) 12 Gyr and (c) 9 Gyr. The observed CMD is plotted in (d). In each panel the contours correspond to densities of 20, 40, 60, 80, 100, 150, 200, 300 and 400 stars decimag $^{-2}$. The SFHs and chemical enrichment histories corresponding to these three model CMDs are plotted in Figure 13.

Fig. 15.— Indicators relative to the color distribution of stars in the brightest RGB region in the H VIII field CMD as a function of the star formation history shape assuming a low initial metallicity of $[\text{Fe}/\text{H}] = -2.3$ ($Z = 0.0001$) and a final metallicity of $[\text{Fe}/\text{H}] = -0.7$ ($Z = 0.004$). (See Figure 10 for the definition of the RGB regions). Note that the SFH shapes are ordered such that they

progress from a dominant young population in Shape 1 to a dominant older population in Shape 5. The median and C95 $V - I$ colors are plotted in panels (a) and (b). The ratio of the number of RGB stars to red clump stars is plotted in (c) while (d) shows the value of $1/\chi^2$ for each model. In each panel, the results are shown separately for T_i of 15 Gyr (dotted line), 12 Gyr (dashed line), 9 Gyr (dot-dashed line) and 6 Gyr (long-dashed line). The solid lines denote the observed value and its probable error due to an uncertainty of ± 0.1 mag in the extinction A_V .

Fig. 16.— Same as Figure 15 except for an initial metallicity of $[\text{Fe}/\text{H}] = -1.0$.

Fig. 17.— The star formation rate (left panels) plotted in units of $10^{-9} M_\odot \text{ yr}^{-1} \text{ pc}^{-2}$ and chemical enrichment history (right panels) for the H VIII field under three different assumptions about the extinction A_V . In the top, middle and bottom panels, the extinction was held fixed at values of $A_V = 0.6, 0.9$ and 1.2 , respectively, while allowing the initial metallicity, final metallicity and enrichment law to vary.

Fig. 18.— The value of the fit parameter as a function of (a) the extinction A_V , (b) the initial metallicity $[\text{Fe}/\text{H}]_i$, (c) the final metallicity $[\text{Fe}/\text{H}]_f$ and (d) the chemical enrichment law, as defined in Figure 6. All SFH solutions plotted here are fits to the H VIII field CMD.

Fig. 19.— The SFR as a function of age derived from the H VIII field CMD under three different assumptions about the chemical enrichment law. The SFH for chemical enrichment laws 1, 2 and 3 are shown in the top, middle and bottom panels, respectively. In each case, the initial and final metallicities are set to $[\text{Fe}/\text{H}] = -2.3$ and -0.9 , respectively.

Fig. 20.— Same as Figure 19, except assuming an initial metallicity of $[\text{Fe}/\text{H}] = -1.4$.

Fig. 21.— Star formation rate (left panels) and chemical enrichment history (right panels) for the H IV, H VI and H VII fields. The SFR is plotted in units of $10^{-9} M_\odot \text{ yr}^{-1} \text{ pc}^{-2}$, averaged over the three WF chips. The metallicities are plotted for the initial and final values in each time bin.

Fig. 22.— Star formation rate (left panels) and chemical enrichment history (right panels) for the H VIII and C25 fields. The SFR is plotted in units of $10^{-9} M_\odot \text{ yr}^{-1} \text{ pc}^{-2}$, averaged over the three WF chips.

Fig. 23.— The SFH of NGC 6822 determined from the H VIII field. The points with error bars are the results determined using the Dolphin (1997) method. The solid and dotted lines correspond to the two best-fitting SFHs determined from the Gallart et al. (1996a) method. The solid line corresponds to SFH shape 4 while the dotted line is SFH shape 3. Both solutions have $T_i = 15$ Gyr and $Z_i = 0.0001$.

Fig. 24.— Recent SFHs for all five fields derived from the main sequence luminosity function (red solid histogram with error bars). For comparison, the recent star formation rates derived from the Dolphin (1997) method are shown as the dotted line with error bars.

Fig. 25.— The locations of the five WFPC2 fields overlayed on the $60\mu\text{m}$ emission measured by the IRAS satellite (Rice 1993). The coordinates are epoch 1950 and the contours correspond to surface brightnesses of 1, 2, 3, 4, 5, 10, 15, 20, 25, 30 and 40 MJy sr^{-1} . The value of the extinction A_V determined from the CMD is shown next to each field. The WFPC2 fields with higher extinction tend to lie in areas of higher IRAS emission.

Fig. 26.— Model CMDs reconstructed from the best-fitting SFHs plotted in Figures 21 and 22. In all panels, the contours correspond to densities of 20,40,60,80,100,150,200,300,400 and 500 stars decimag^{-2} . (See Figure 2 for the observed CMDs).

Fig. 27.— Grayscale Hess images showing the difference between the observed and model Hess diagrams divided by the model diagram for each of the five fields. In each panel white corresponds to more model stars than observed stars. The ratio has been plotted from a value of -1.5 (white) to $+1.5$ (black).

Fig. 28.— Integrated absolute rest-frame B (solid line) and V (dotted line) magnitudes for NGC 6822 as a function of look-back time. The curves were calculated from the SFH for the H VIII field using the PEGASE galaxy evolution code (Fioc & Rocca-Volmerange 1997). The upper x-axis shows the redshift corresponding to each age on the bottom axis assuming a flat cosmology with a Hubble constant $H_0 = 75 \text{ km/s/Mpc}$ and $\Omega_\Lambda = 0.7$.

Table 1. Summary of observations

Field	File	Filter	Exp. time (sec)	Date of obs.
H IV	u37h0201r.c0h	F555W	2600	1999 July 21
	u37h0202r.c0h	F555W	1300	1999 July 21
	u37h0203r.c0h	F814W	2700	1999 July 21
	u37h0204r.c0h	F814W	1200	1999 July 21
H VI	u37h0301r.c0h	F555W	2487	1999 March 24
	u37h0302r.c0h	F555W	1300	1999 March 24
	u37h0303r.c0h	F814W	2700	1999 March 24
	u37h0304r.c0h	F814W	1200	1999 March 24
H VII	u37h0401r.c0h	F555W	2600	1999 March 26
	u37h0402r.c0h	F555W	1300	1999 March 26
	u37h0403r.c0h	F814W	2700	1999 March 27
	u37h0404r.c0h	F814W	1200	1999 March 27
H VIII	u37h0501r.c0h	F555W	2600	1999 March 29
	u37h0502r.c0h	F555W	1300	1999 March 29
	u37h0503r.c0h	F814W	2700	1999 March 29
	u37h0504r.c0h	F814W	1200	1999 March 29
C25	u5ch0403r.c0h	F555W	800	1999 September 24
	u5ch0404r.c0h	F555W	400	1999 September 24
	u5ch0405r.c0h	F814W	600	1999 September 24
	u5ch0406r.c0h	F814W	600	1999 September 24

Table 2. Comparison of H VI and H VII photometry

Chip					
H VI	H VII	ΔV	σ_V	ΔI	σ_I
WF2	PC	−0.046	0.127	−0.029	0.092
WF2	WF2	0.016	0.085	0.000	0.061
WF3	PC	−0.050	0.190	−0.076 ^a	0.199
WF3	WF2	0.011	0.068	−0.043	0.063
WF3	WF3	0.003	0.081	−0.034	0.073
WF3	WF4	0.000	0.093	−0.009	0.070
WF4	WF4	−0.006	0.079	0.010	0.067

^aAverage is affected by a few discrepant bright stars

Table 3. Parameters used to solve for the SFH

Parameter	Minimum	Maximum	Step
A_V	0.6	1.3	0.1
$[Fe/H]_i$	−2.3	−1.4	0.3
$[Fe/H]_f$	−1.1	−0.7	0.2
Fixed Parameters			
$(m - M)_0$	23.49		
α	1.35		
binary fraction	0.0		
$\sigma([Fe/H])$	0.0		

Table 4. SFH Solutions for the H VIII Field for $T_i = 15, 11, 8$ Gyr

Fit parameter				
T_i (Gyr)	Min	Max	Num. of solutions	A_V
15	3.19	3.50	30	0.817 ± 0.072
12	3.25	3.65	32	0.824 ± 0.076
9	3.35	3.85	32	0.839 ± 0.076

Table 5. SFRs for the H VIII Field for $T_i = 15, 12, 9$ Gyr

SFR ($10^{-9} M_\odot \text{ yr}^{-1} \text{ pc}^{-2}$)			
Age (Gyr)	$T_i = 15$ Gyr	$T_i = 12$ Gyr	$T_i = 9$ Gyr
0.001 – 0.2	6.1 ± 0.7	6.4 ± 1.0	6.4 ± 1.0
0.2 – 0.6	4.7 ± 3.6	4.7 ± 0.4	4.8 ± 0.3
0.6 – 3	7.3 ± 0.9	7.0 ± 1.1	6.8 ± 1.6
3 – 5	0.05 ± 0.16	1.4 ± 2.7	6.0 ± 3.6
5 – 7	6.2 ± 3.5	5.7 ± 4.4	0.7 ± 2.1
$7 - T_i$	2.6 ± 1.7	3.4 ± 2.5	6.4 ± 4.9

Table 6. SFH solutions for the Five *HST* Fields

Fit parameter				
Field	Min.	Max.	Num. of solutions	A_V
H IV	3.54	3.80	31	1.041 ± 0.070
H VI	5.00	5.40	33	1.090 ± 0.071
H VII	4.71	5.16	32	1.019 ± 0.069
H VIII	3.19	3.50	30	0.817 ± 0.072
C25	2.28	2.80	28	0.720 ± 0.073

Table 7. SFRs for the Five *HST* Fields

Age (Gyr)	SFR ($10^{-9} M_{\odot} \text{ yr}^{-1} \text{ pc}^{-2}$)				
	H IV	H VI	H VII	H VIII	C25
0.001 – 0.2	14.5 ± 1.7	25.4 ± 3.4	18.0 ± 2.6	6.1 ± 0.7	3.8 ± 0.3
0.2 – 0.6	8.8 ± 1.0	21.4 ± 2.7	18.3 ± 1.7	4.7 ± 0.4	3.4 ± 0.5
0.6 – 3	8.1 ± 1.0	13.4 ± 2.2	11.8 ± 1.7	7.3 ± 0.9	8.6 ± 1.2
3 – 5	0.0 ± 0.0	0.1 ± 0.5	0.0 ± 0.3	0.1 ± 0.2	0.2 ± 0.2
5 – 7	7.5 ± 3.4	12.4 ± 5.7	10.9 ± 4.6	6.2 ± 3.5	10.3 ± 4.8
7 – 15	3.7 ± 2.1	4.1 ± 3.0	7.6 ± 2.8	2.6 ± 1.7	1.4 ± 1.3

This figure "wyder.fig1.jpg" is available in "jpg" format from:

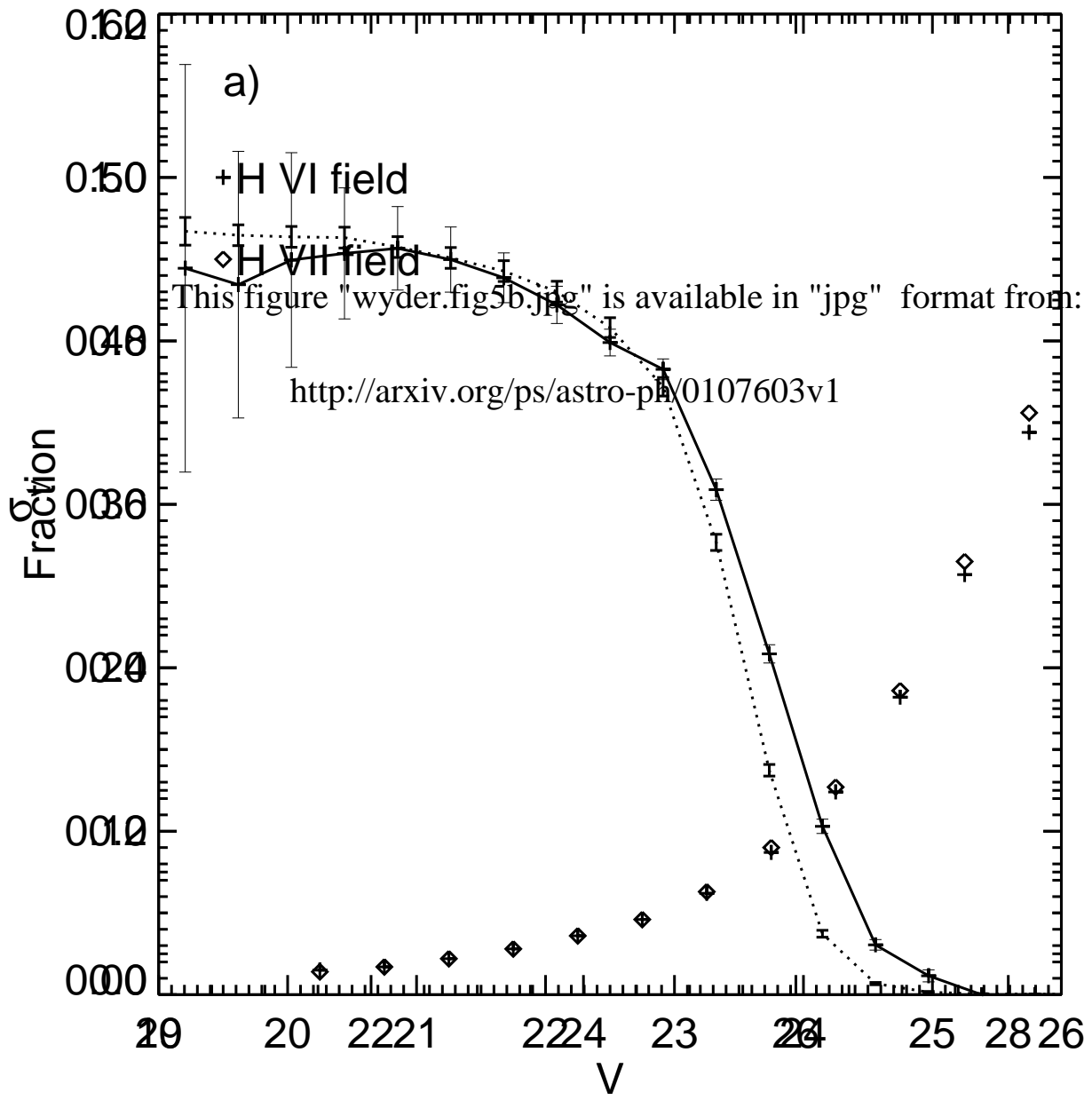
<http://arxiv.org/ps/astro-ph/0107603v1>

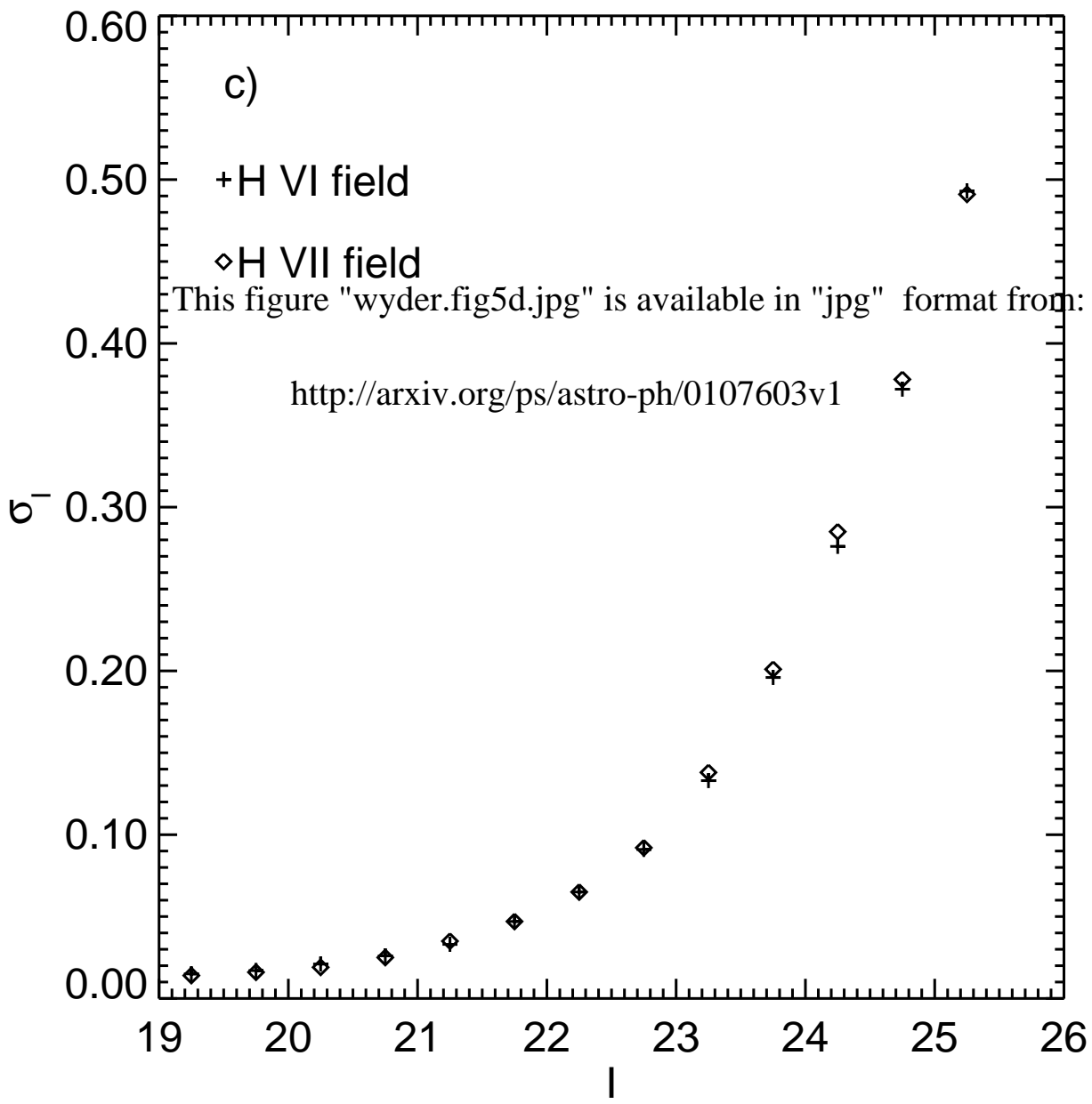
This figure "wyder.fig2.jpg" is available in "jpg" format from:

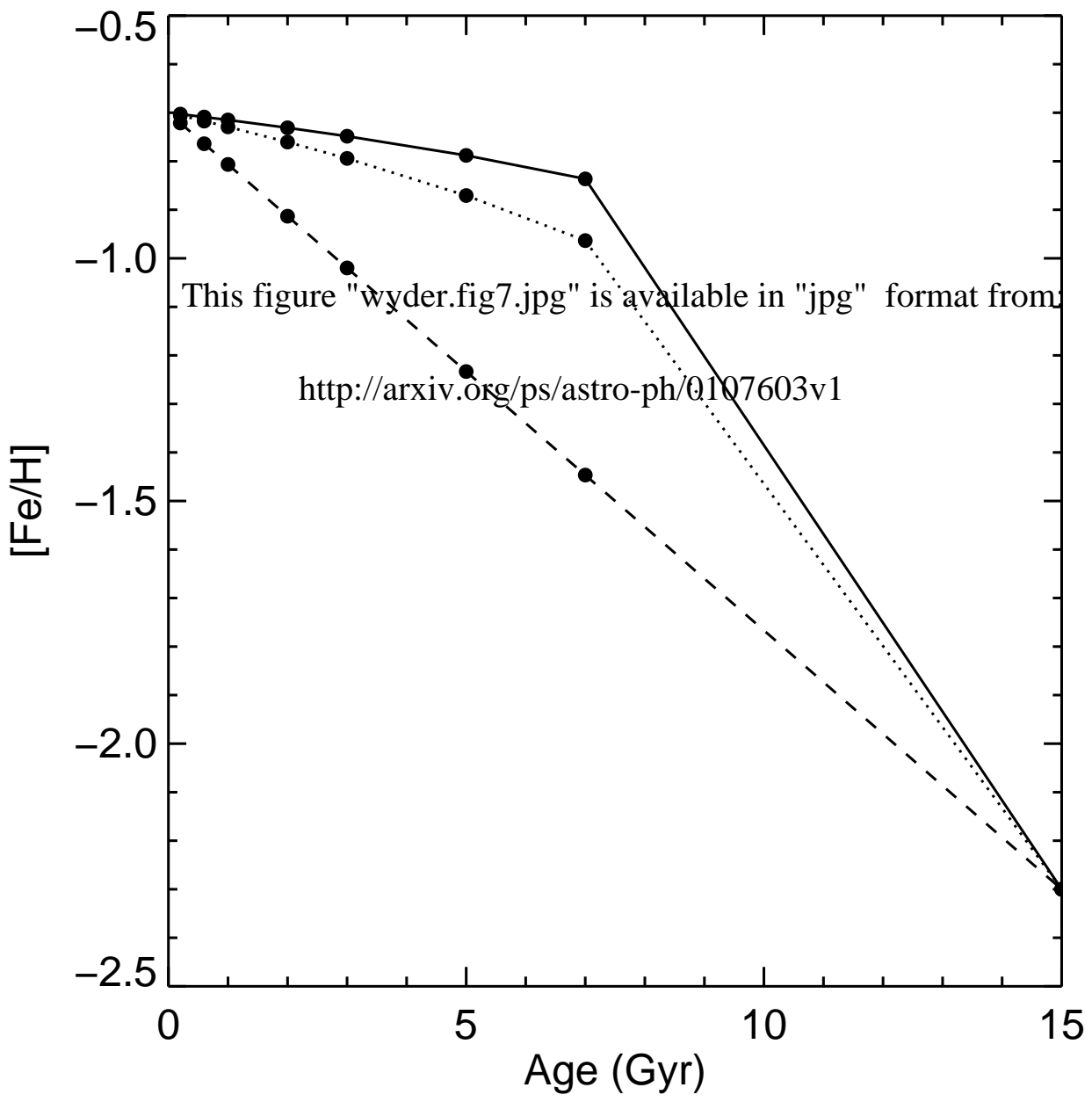
<http://arxiv.org/ps/astro-ph/0107603v1>

This figure "wyder.fig3.jpg" is available in "jpg" format from:

<http://arxiv.org/ps/astro-ph/0107603v1>

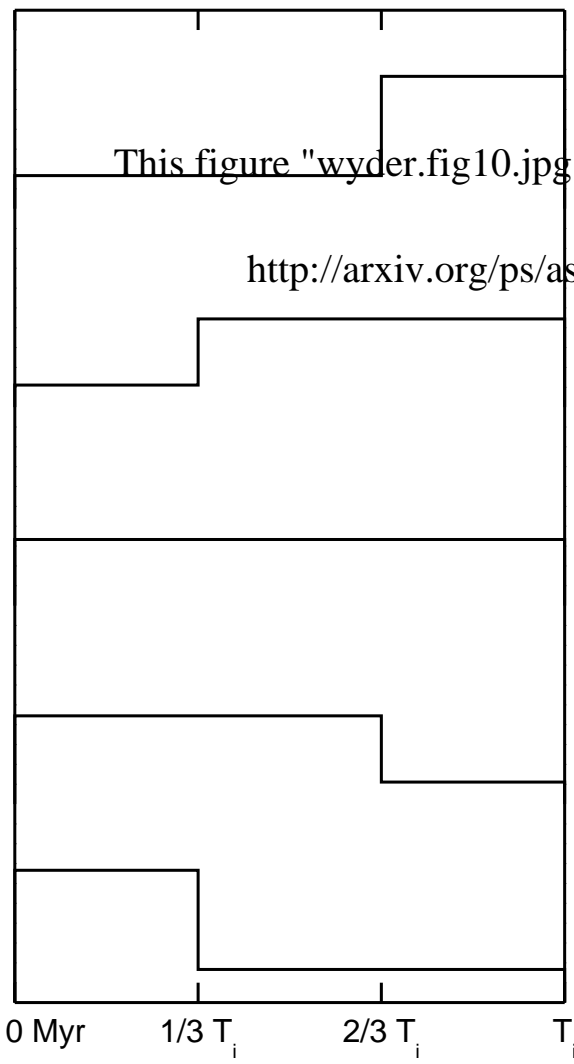






This figure "wyder.fig8.jpg" is available in "jpg" format from:

<http://arxiv.org/ps/astro-ph/0107603v1>



This figure "wyder.fig10.jpg" is available in "jpg" format from:

<http://arxiv.org/ps/astro-ph/0107603v1>

This figure "wyder.fig11.jpg" is available in "jpg" format from:

<http://arxiv.org/ps/astro-ph/0107603v1>

This figure "wyder.fig12.jpg" is available in "jpg" format from:

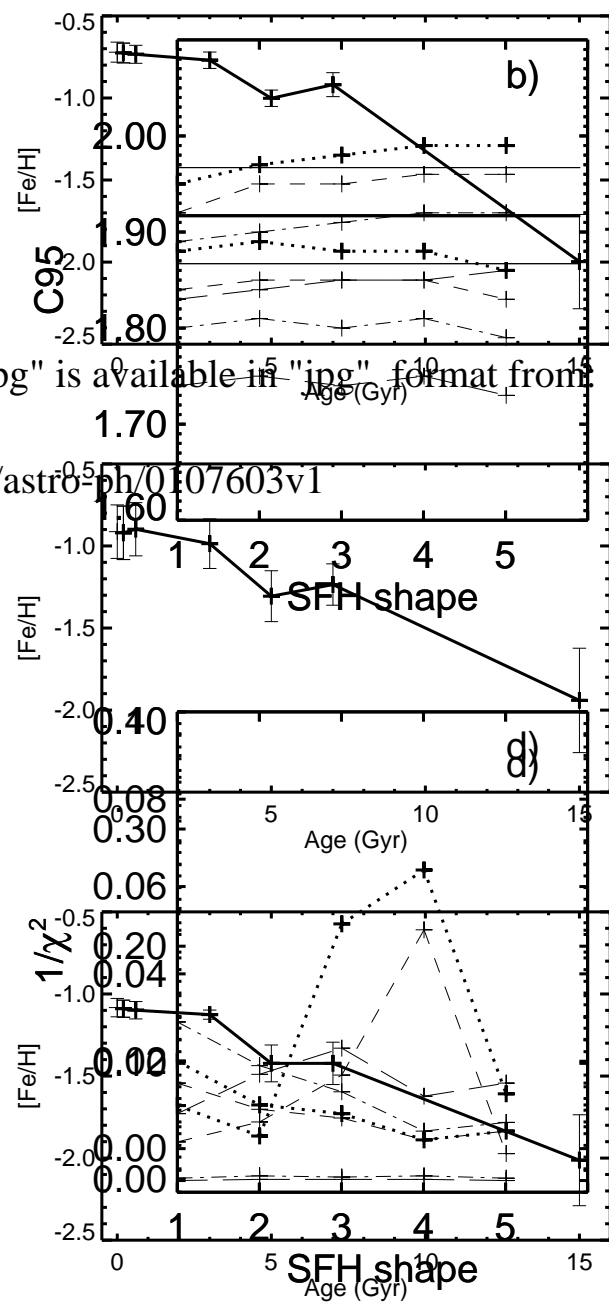
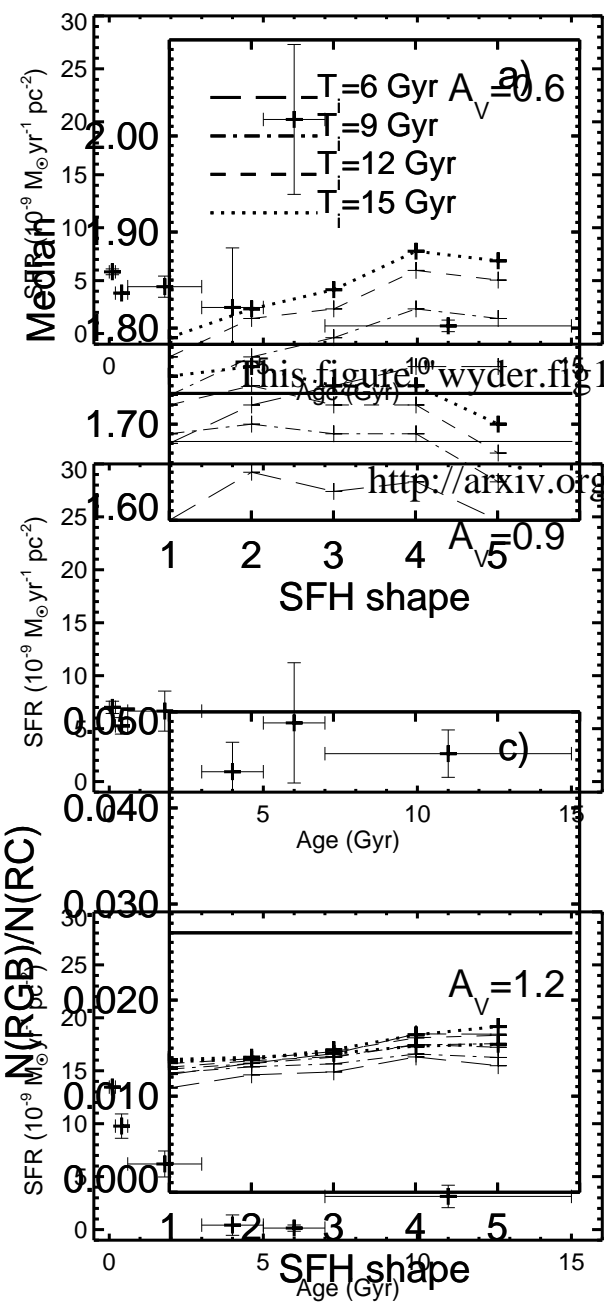
<http://arxiv.org/ps/astro-ph/0107603v1>

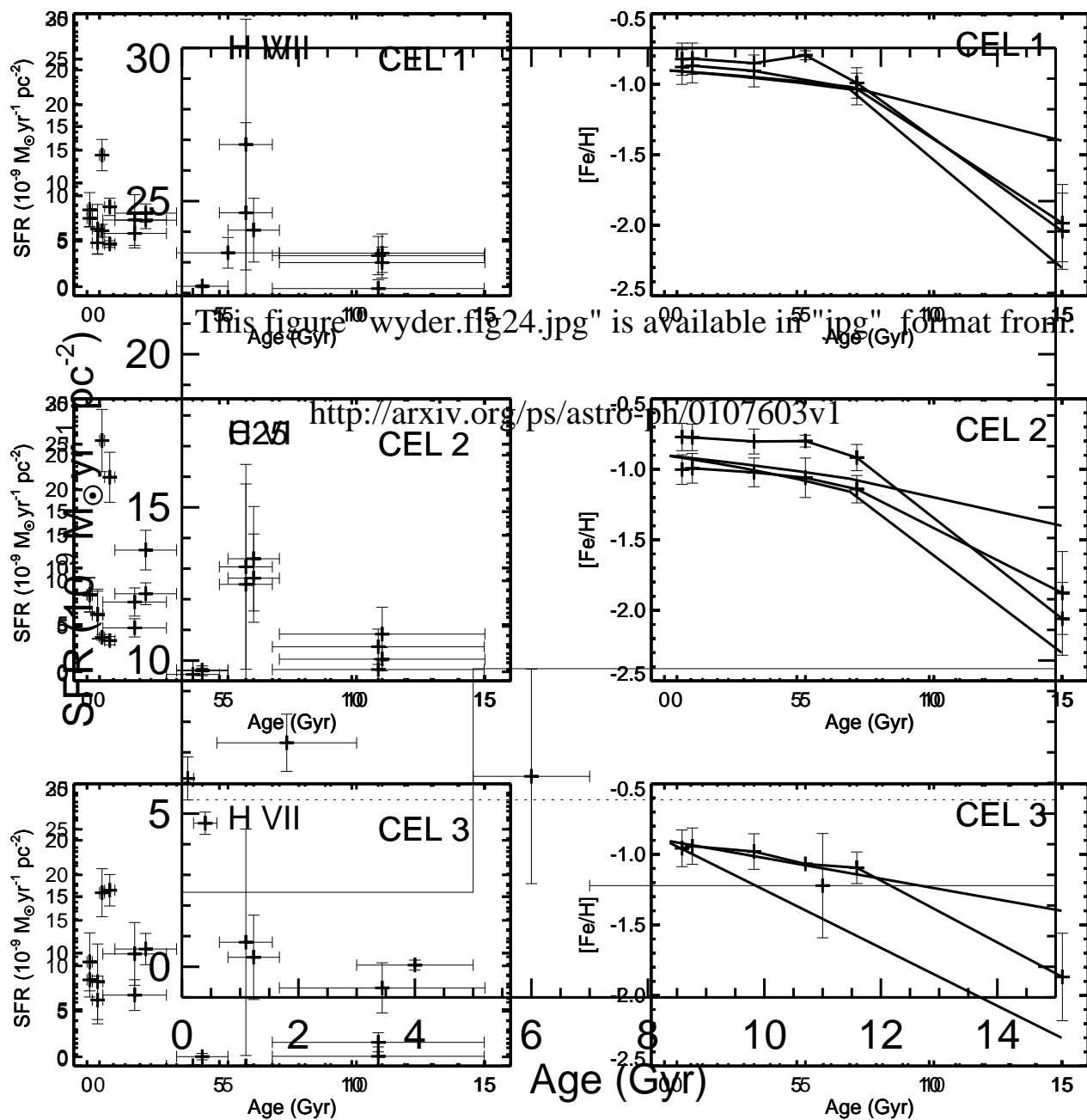
This figure "wyder.fig13.jpg" is available in "jpg" format from:

<http://arxiv.org/ps/astro-ph/0107603v1>

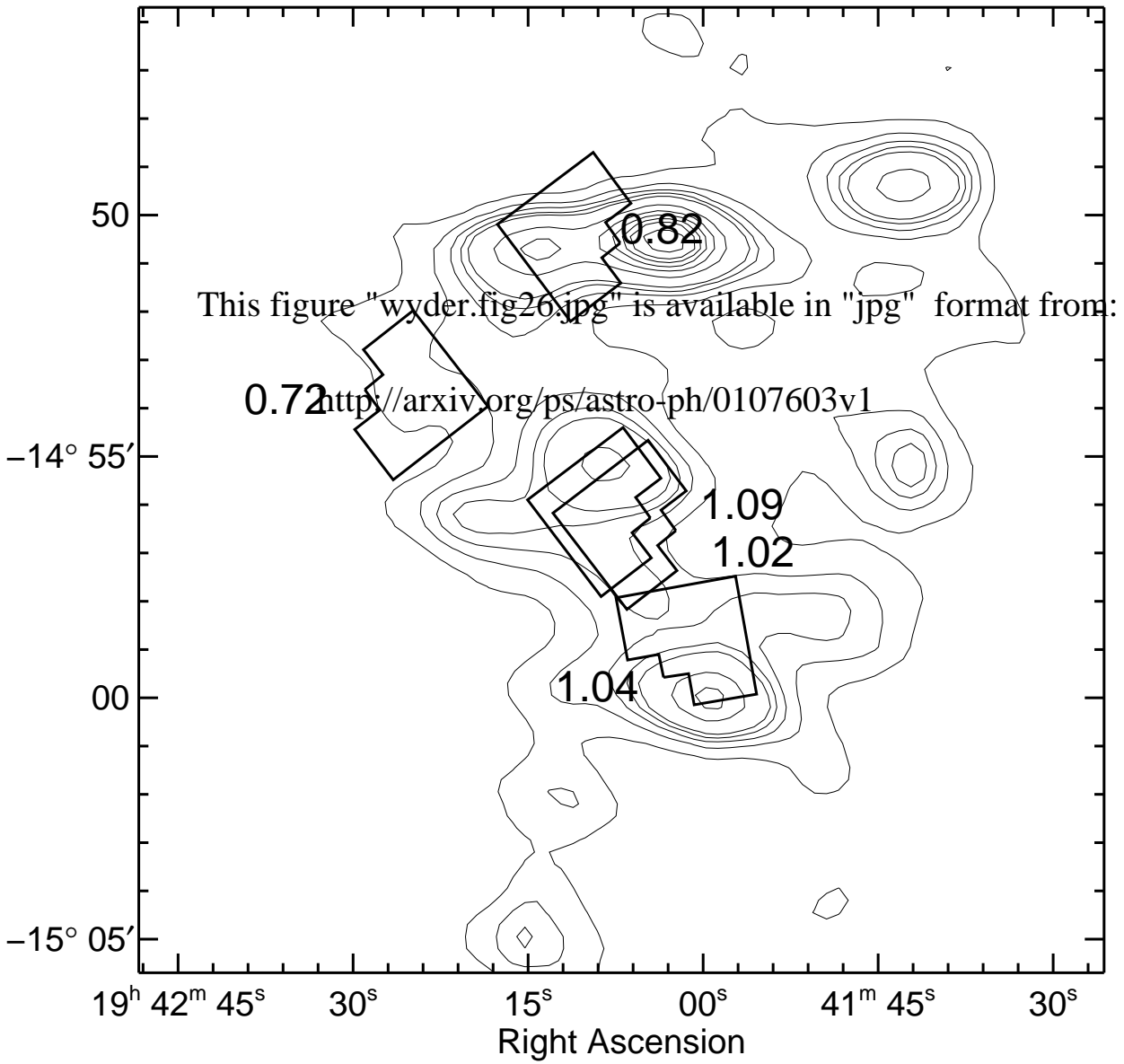
This figure "wyder.fig14.jpg" is available in "jpg" format from:

<http://arxiv.org/ps/astro-ph/0107603v1>





Declination



This figure "wyder.fig27.jpg" is available in "jpg" format from:

<http://arxiv.org/ps/astro-ph/0107603v1>